

See discussions, stats, and author profiles for this publication at: <https://www.researchgate.net/publication/384297877>

Unsteady Loads of a Scaled Rotor on and Near the Landing Deck of the NATO Generic Destroyer with Concurrent Stereo PIV and Surface Pressure Measurements

Article in Journal of the American Helicopter Society · October 2024

DOI: 10.4050/JAHS.69.042008

CITATIONS

7

2 authors:



Wei-Han Chen
Georgia Institute of Technology

7 PUBLICATIONS 28 CITATIONS

[SEE PROFILE](#)

READS

126



Juergen Rauleder
Georgia Institute of Technology

102 PUBLICATIONS 609 CITATIONS

[SEE PROFILE](#)

Unsteady Loads of a Scaled Rotor on and Near the Landing Deck of the NATO Generic Destroyer with Concurrent Stereo PIV and Surface Pressure Measurements



Wei-Han Chen*
Doctoral Candidate
Georgia Institute of Technology, Atlanta, GA



Juergen Rauleder
Assistant Professor
Georgia Institute of Technology, Atlanta, GA

This work is licensed under Creative Commons Attribution International License CC-BY

Rotorcraft shipboard operations are risky and demand high piloting skills. To gain further understanding and familiarize pilots with these complicated scenarios, various methods of computational simulations have been used in the past decades. Yet, some simulation methods may not capture a realistic response of the rotorcraft due to simplified modeling of the interactional aerodynamics in order to achieve real-time capability for pilot training. Thus, improvements to these simulations are required, and experimental data that unveil the interactional aerodynamics and dynamics between the rotor and ship are needed for computational validation efforts. In this study, an extensive experimental investigation of the ship–rotor dynamic interface problem was conducted to gain a general understanding of the interactional aerodynamics between a 1:100 wind-tunnel-scale NATO Generic Destroyer and a representative single main rotor, operating both stationary and dynamically moving in space in the vicinity of the landing deck. Data obtained through simultaneous measurements of rotor hub loads, ship deck surface pressures, and stereoscopic particle image velocimetry flow fields gave valuable insight into the highly coupled aerodynamic phenomena. Results showed that the rotor hub loads exhibited a high dependency on both the wind direction and also the position of the rotor relative to the landing deck. A bifurcation in the regions of high unsteady thrust was observed under certain wind conditions due to the ship airwake, impacting different portions of the rotor disk. The inflow angles across the rotor disk were estimated and assessed through flow field measurement, revealing how the ship airwake altered the rotor inflow and wake structure that contributed to the unique change in rotor loads under various hovering conditions.

Nomenclature

A_f	accumulated frontal area of the test article, m ²	N_b	number of rotor blades
A_t	test section cross-sectional area, m ²	p	surface pressure, Pa
C_T	thrust coefficient, $\frac{T}{\rho(\pi R^2)(\Omega R)^2}$	p_o	reference pressure, Pa
C_{Mx}	rolling moment coefficient, $\frac{M_x}{\rho(\pi R^2)(\Omega R)^2 R}$	q_u, q_c	uncorrected and corrected dynamic pressure, Pa
C_{My}	pitching moment coefficient, $\frac{M_y}{\rho(\pi R^2)(\Omega R)^2 R}$	R	rotor radius (m)
C_p	pressure coefficient, $\frac{p-p_o}{q_c}$	Re_s	ship beam Reynolds number, $\frac{U_\infty w_s}{v}$
c	blade chord, m	Re_{tip}	rotor blade tip Reynolds number, $\frac{U_{tip} c}{v}$
F_x, F_y, F_z	rotor longitudinal, lateral, and axial force, N	r	rotor radial location, m
h	height above the landing deck, m	T	thrust, N
h_{hod}	height at hover-over-deck, m	\tilde{T}_{rms}	normalized unsteady thrust, $\frac{T_{rms}}{T}$
\tilde{k}	normalized turbulent kinetic energy, $\frac{0.5(\bar{u}^2 + \bar{v}^2 + \bar{w}^2)}{U_\infty^2}$	t	time after rotor reached hover-over-deck, s
M_x, M_y, M_z	rotor rolling, pitching, and yawing moment, N·m	U_∞	freestream velocity, m/s
M_{tip}	rotor blade tip Mach number	U_P, U_T	normal and tangential inflow velocities in the rotor frame, m/s
		\tilde{U}_P, \tilde{U}_T	normalized normal and tangential inflow velocities in the rotor frame, $\frac{U_P}{U_\infty}, \frac{U_T}{U_\infty}$
		u, v, w	velocities in x , y , and z directions, m/s
		$\bar{u}, \bar{v}, \bar{w}$	mean velocities in x , y , and z directions, m/s
		$\tilde{u}, \tilde{v}, \tilde{w}$	normalized mean velocities in x , y , and z directions, $\frac{\bar{u}}{U_\infty}, \frac{\bar{v}}{U_\infty}, \frac{\bar{w}}{U_\infty}$
		u', v', w'	velocity fluctuations in x , y , and z directions, m/s

*Corresponding author; email: wchen669@gatech.edu.

A previous version of this paper was presented at the Vertical Flight Society's 80th Annual Forum & Technology Display, Montreal, Quebec, Canada, May 7–9, 2024. Manuscript received May 2024; accepted September 2024.

V	velocity magnitude, m/s
\tilde{V}	normalized velocity magnitude, $\frac{V}{U_\infty}$
V_{app}	rotor approach velocity, m/s
w_s, l_s	width and length of ship, m
x, y, z	longitudinal, lateral, and vertical positions, m
μ	advance ratio, $\frac{U_\infty}{\Omega R}$
ν	kinematic viscosity, m^2/s
ρ	air density, kg/m^3
σ	rotor solidity, $\frac{N_b c}{\pi R}$
Ψ	rotor azimuth angle, deg
ψ	wind-over-deck angle, deg
Ω	rotor angular velocity, rad/s

Introduction

Rotorcraft shipboard operations are known to be extremely challenging, even for highly skilled helicopter pilots. Under a relative wind, the unsteady airwake shed from the ship superstructure can greatly influence the forces exerted on the airframe and also disturb the rotor inflow, causing highly unsteady aerodynamic interactions, often referred to as the ship–rotor dynamic interface (DI). These interactions result in continuously varying aerodynamic loads on the vehicle, which can be difficult for the pilots to counteract and maintain a stable flight attitude. In some circumstances, they limit the conditions under which the rotorcraft can be safely launched and/or recovered from the ship. Especially at higher sea states, the strong winds accompanied by the large motions of the ship deck can greatly compromise the handling qualities of the rotorcraft.

In the past decades, researchers have approached the DI problem with extensive experimental and computational efforts. These subscale experiments provided low-risk and quick-turnaround means to explore the unsteady aerodynamic phenomena and also provided valuable validation information for modeling and simulations. One of the earlier efforts was from Lee and Zan (Refs. 1, 2) through wind tunnel experiments with a 1:50-scale model of the Canadian Patrol Frigate (CPF). It has been shown that interactions between the rotor and the ship airwake could greatly degrade the rotor performance. Additionally, the significance of influence varied as the rotor position above the landing deck was changed (Ref. 1). They also demonstrated that the characteristics of the ship–rotor interactional effects had a strong dependence on the wind direction and wind speed over the ship. Additional efforts were made to quantify the unsteady loads acting on the helicopter model airframe, and a positive correlation was found between the unsteady loads and pilot workload from flight test data (Refs. 2, 3).

Silva et al. (Ref. 4) carried out experimental investigations of the aerodynamic interactions between rotorcraft around a 1:48-scale Landing Helicopter Assault class ship. The effort was motivated by a shipboard incident in which an on-deck V-22 experienced an uncommanded roll in response to a CH-46 being recovered upwind. This effort involved multiple rotorcraft models, including the V-22 Osprey, CH-46 Sea Knight, and the CH-53E Super Stallion. An intensive survey with loads and particle image velocimetry (PIV) measurements showed strong dependencies in the on-deck tiltrotor rolling moment response to the relative position of the upwind aircraft and wind-over-deck (WOD) conditions.

Wang et al. (Ref. 5) introduced a different experimental setup in a water tunnel. A custom-designed six-component dynamic force balance was constructed for the 1:54-scale Merlin helicopter model to assess the impact of the unsteady airwake generated by the ship. A water tunnel was preferred over a traditional wind tunnel mainly due to the relative ease of generating a higher Reynolds number that was more relevant to a full-scale condition. Additionally, the water tunnel allowed

for ease of flow visualization through PIV measurements. Kääriä et al. (Ref. 6), using the same experimental setup, explored how different designs of the ship superstructure impacted the performance of a rotor operating in the ship wake. Various modifications to the ship superstructure were demonstrated to have a positive effect on reducing the unsteady rotor loads along the side-step approach path from the port side of the ship.

Recently, a detailed investigation was performed by Silva et al. (Ref. 7) on V-22 and H-1 rotorcraft models operating behind a 1:48-scale San Antonio class landing platform dock (LPD) ship. Extensive loads, PIV, and surface pressure measurements were carried out with the rotorcraft operating at different locations and orientations around the landing deck of the LPD model in various wind directions. Results showed trends of the thrust deficit behind the ship superstructure and also variations in the differential thrust controls required to compensate for the induced rolling moment on the V-22 model. The rich information collected was used as a source of truth data for modeling and simulation validation in the U.S. Navy.

In order to gain a more general understanding and allow a certain degree of comparability across different research efforts, the simplified frigate shape (SFS), a representative ship geometry that resembles a naval frigate, was also used across multiple studies. Zhu et al. (Ref. 8) and Mazzilli et al. (Ref. 9) investigated the airwake features of the SFS geometry through PIV and explored its unique bistable behavior through a dual-plane synchronous PIV technique. Palm et al. (Ref. 10) also assessed the SFS wake dynamics but under quartering winds, leveraging proper orthogonal decomposition and conditional averaging of the measured flow field. All of these studies were for an isolated ship (i.e., no rotor).

Nacakli et al. (Ref. 11) studied the ship–rotor coupled flow field using a backward-facing-step as a representative ship, similar to the SFS geometry. A PIV survey was conducted with thrust measurements of a rotor hovering at various positions above the landing deck along the symmetric plane of the ship in a headwind. It was observed that the competing effect between the reingestion of the recirculated flow close to the hangar wall and the ground effect significantly influenced the rotor thrust. These influences greatly increased as the distance downstream from the hangar wall was reduced. Lateral PIV measurements also indicated asymmetries in the rotor downwash and the significance varied as the height above the deck was altered. Also using the SFS ship geometry, Taymourtash et al. (Ref. 12) assessed the loads on a 1:13-scale Bo105 helicopter model in various positions along a stern approach and a vertical descent trajectory. They observed significant changes both in pitching and rolling moments along the path, but the degree of variation was highly dependent on the wind direction.

Computationally, researchers have utilized and compared different computational fluid dynamics (CFD) solvers to model the SFS-2 airwake (Ref. 13) and also assessed the impact of the SFS-2 ship airwake on helicopter handling qualities (Ref. 14).

Although being simple and widely used, the SFS geometry still lacks many significant geometric features of a modern naval vessel. Recently, the NATO Generic Destroyer (NATO-GD), shown in Fig. 1, was introduced as a shared geometry for collaborative research by the Canadian National Research Council towards a more generalized understanding and accurate modeling and simulation of the ship–rotor dynamic interface problem (Ref. 15). The NATO-GD is symmetric about the longitudinal centerplane with the inclusion of several additional features on the superstructure which resembles a more realistic geometry. It has been computationally shown that the NATO-GD produced dissimilar airwakes compared with the SFS and interacted differently with a helicopter (Ref. 16). As of today, although there is an appreciable amount of computational effort modeling the ship–rotor dynamic interface of the

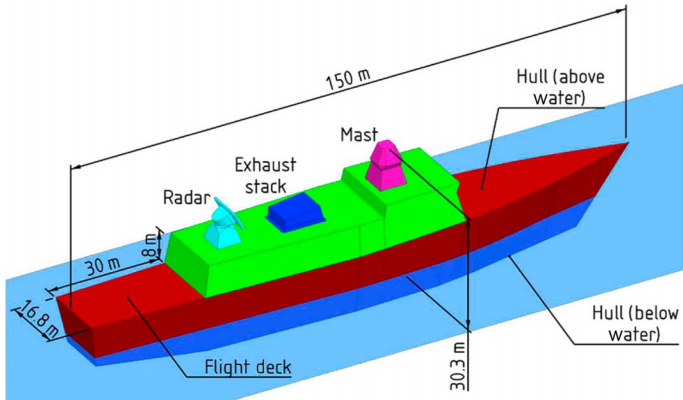


Fig. 1. The NATO generic destroyer (Ref. 15).

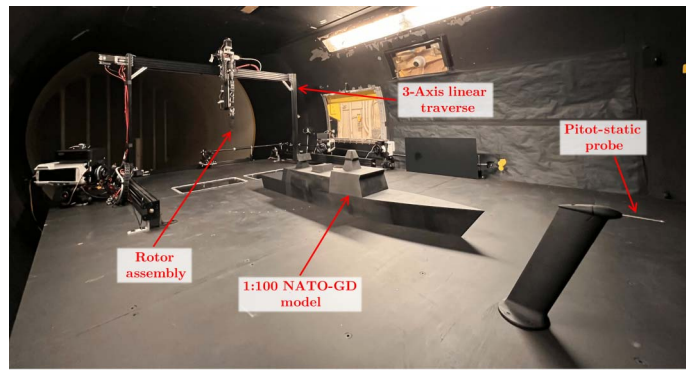


Fig. 2. Experimental setup in the wind tunnel.

NATO-GD through different fidelity approaches (Refs. 17, 18), there is still limited experimental research available on the NATO-GD to validate these computational efforts; see, for example, Fernandez et al. (Ref. 19).

Currently, the most widely used computational technique is the one-way coupled approach (Refs. 14, 20, 21) where the unsteady ship airwake is first evaluated without the presence of the rotorcraft. Then, the precomputed ship airwake is superimposed with the real-time piloted simulation, which modifies the rotor inflow. However, this approach is unable to capture the true physics of the interactional phenomena due to the fact that the rotor does not alter the ship airwake. As a result, the recirculation and ground effect cannot be represented correctly. To accurately simulate the response of rotorcraft for pilot training, real-time capable two-way coupled simulations are needed. At the same time, experimental results play a critical role in the validation of these efforts.

In the current study, subscale wind tunnel experiments were conducted that simultaneously measured rotor hub loads, ship surface pressures, and stereoscopic PIV flow fields. A series of different test configurations were deployed targeting a detailed investigation of the aerodynamic characteristics of a representative rotorcraft with a single main rotor operating in the vicinity of the NATO-GD landing deck, both while fixed in space and moving dynamically. Tests were conducted under various freestream wind velocities and WOD angles. Additionally, in support of the validation of computational efforts, a subset of the results obtained from this current study have already been used as validation data for a two-way coupled mid-fidelity GPU-accelerated lattice-Boltzmann real-time model by Ashok and Rauleder (Ref. 22).

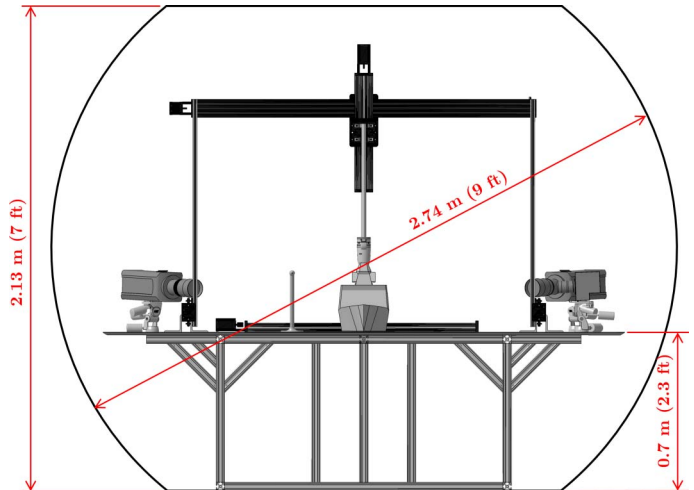


Fig. 3. Drawing (frontal view) of the experimental setup in the wind tunnel.

Methodology

Experiments were conducted in the John J. Harper Memorial Wind Tunnel at the Georgia Institute of Technology. The wind tunnel is a subsonic closed-return type tunnel with a semicircular test section that measures 2.74 m (9 ft) in diameter and 2.13 m (7 ft) in height. A custom test rig was designed and built on an elevated platform that was positioned 0.7 m (2.3 ft) above the tunnel floor, as shown in Figs. 2 and 3. This leveraged the partially circular nature of the tunnel cross section and provided better clearance to the walls, thus reducing possible wall interference during experiments. A three-axis automated traverse system driven by integrated servo motors with feedback control was installed on top of the elevated platform and downstream of the ship model for accurate positioning and speed control of the rotor. Linear magnetic encoders were installed on each traverse axis such that the spatial position of the rotor hub could be tracked by the data acquisition system.

Ship model

The ship model was a 1:100 scale NATO-GD manufactured with polylactic acid through fused deposition modeling three-dimensional (3D) printing. A matte black paint was applied to the surface of the aft section of the ship model to minimize the reflection from the laser during PIV flow field measurements. The model was made in sections with an internal cavity and access panels to house the instrumentation for surface pressure measurements.

Surface pressures on the landing deck and hangar wall were measured through 126 pressure taps (98 on the landing deck and 28 on the hangar wall, shown in Fig. 4) connected to two 64-channel differential pressure scanners from Surrey Sensors (± 160 Pa full-scale range; 14-bit resolution; uncertainty $\pm 0.25\%$ full scale). Housing the pressure scanners inside the model minimized the pressure tube length between the surface taps and the sensor module, ensuring adequate response characteristics. Screw holes were drilled on the elevated platform as mounting points to fix the ship model at yaw angles (ψ) up to 60 deg with 5-deg increments in both directions to achieve different WOD conditions. These mounting points were located in a way such that the center of the ship landing deck stayed fixed when yawed.

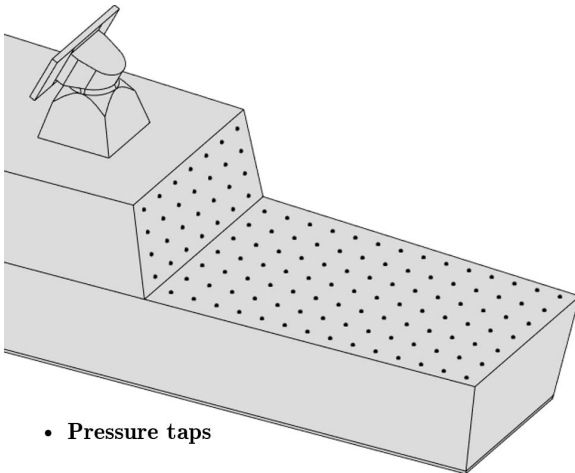


Fig. 4. Pressure tap distribution on the ship model.

Rotor model

The rotor model (Fig. 5) had a hingeless rotor hub which was modified from a commercial off-the-shelf two-bladed radio-controlled helicopter rotor with a fully servo-controlled swashplate assembly providing both collective and cyclic controls. The rotor blades were rectangular, untwisted, and without taper. Each blade had a radius (R) of 0.103 m and a chord length (c) of 0.015 m with a 9% thickness-to-chord ratio symmetric airfoil. The rotor was driven counterclockwise by a T-motor AS2317 KV1250 brushless DC motor with an electronic speed controller (ESC) and a 12-V DC power supply.

A magnetic rotary encoder with a resolution of 2048 ticks per revolution was installed behind the brushless motor to track the rotor azimuthal position, enabling phase-correlated measurements. The entire assembly was attached to a Nano17 six-component force/torque transducer from ATI Industrial Automation for rotor hub load measurements. The calibrated range and uncertainty of the transducer are listed in Table 1.

To prevent the aerodynamic forces and moments of the rotor support structure from contaminating the load measurements, a 3D-printed aerodynamic shroud was designed to attach to the nonmeasuring side of the transducer and enclose the entire rotor assembly, leaving only the rotor hub exposed to the freestream. The voltage signals from the transducer were amplified through an interface and power supply unit and sampled through a dSPACE MicroLabBox with 16-bit resolution.

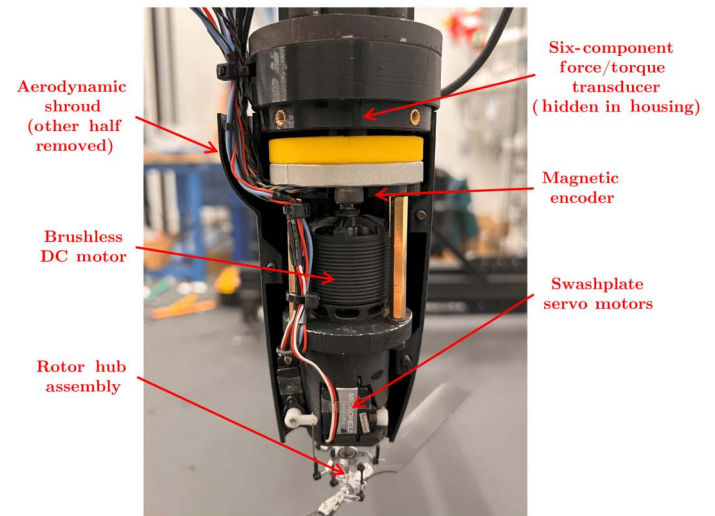
The rotor angular rate and swashplate trim control were also integrated into the dSPACE system. The rotor angular rate was maintained through a proportional-integral-derivative (PID) controller, which used the filtered signal from the rotary encoder on the rotor assembly as input and output a pulse-width modulation signal to the ESC of the brushless motor. Trimming the rotor was accomplished through an auto-trim function also based on a PID controller using the filtered load measurements. The trim controller was designed to maintain the target thrust (T) value and near-zero rolling and pitching moments (M_x , M_y) by manipulating the collective and cyclic controls of the swashplate.

Scaling parameters

Table 2 lists the comparison of velocities, geometric dimensions, and scaling parameters in full scale and model scale. The referenced full-scale rotocraft in this study was the NATO Generic Rotorcraft (NATO-GR), which has geometric dimensions based on the SH-60



(a) External view



(b) Internal view

Fig. 5. The rotor assembly.

Table 1. Calibrated range and uncertainty of the Nano17

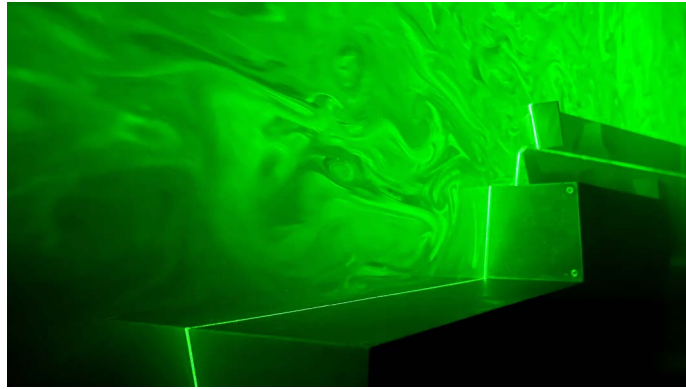
	Range	Uncertainty (95% CI)
F_x , F_y	3 lbf (13.3 N)	1%
F_z	4.25 lbf (18.9 N)	1.25%
M_x , M_y	1 lbf-inch (11.3 N-cm)	1.5%
M_z	1 lbf-inch (11.3 N-cm)	1.75%

Seahawk. The gross weight of the NATO-GR is 7000 kg (15,432 lb), as described in the NATO AVT-315 group report (Ref. 23). However, matching all dimensionless parameters in a subscaled wind tunnel experiment is difficult. Thus, a compromise was made by only matching rotor μ and C_T , but not Re_s . This was done because it has been shown in several studies (Refs. 24, 25) that a ship airwake was essentially insensitive to Reynolds number at sufficiently high ship beam Reynolds numbers (Re_s) due to the nature of its bluff body with sharp edges. In these studies, it was observed through experiments that this Reynolds number insensitivity was true above a ship beam Reynolds number in the range of 10^4 – 10^5 .

In this current study, the test condition resulted in a Re_s of 7.6×10^4 , which is close to the higher end of the threshold suggested by the above-mentioned studies. This provided confidence that, although the Reynolds

Table 2. Testing conditions and scaling parameters

	Reference Condition at Full Scale	Wind Tunnel Model Scale
U_∞	40 kt (20.6 m/s)	5 m/s
l_s	150 m	1.5 m
w_s	22.1 m	0.221 m
Re_s	3.1×10^7	7.6×10^4
R	8.2 m	0.103 m
c	0.527 m	0.015 m
σ	0.08	0.093
Ω	27.0 rad/s (258 RPM)	521.3 rad/s (4,978 RPM)
M_{tip}	0.64	0.16
Re_{tip}	8.0×10^6	5.5×10^4
μ		0.093
C_T		0.0058 (out-of-ground effect)

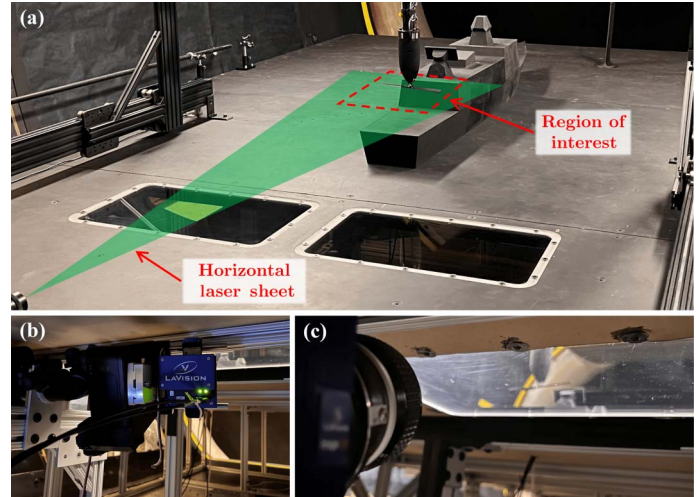
**Fig. 6. Vertical laser sheet illuminating seeding particles above the landing deck.**

number was not matched, the characteristics of the airwake produced by the ship were similar to that in full scale. Additionally, the rotor solidity (σ) was of similar magnitude, giving a similar rotor blade loading coefficient (C_T/σ); see Table 2. However, the blade-tip conditions, M_{tip} and Re_{tip} , of the model were not possible to match the full-scale reference. Therefore, one should keep in mind that the compressibility effects close to the tip of the rotor were likely not accurately scaled.

Particle image velocimetry

Flow field measurements were performed using three-component stereoscopic particle image velocity. Two different configurations were used to measure the velocity fields in this study: one for the horizontal rotor outflow plane and the other for the streamwise-vertical planes (hereinafter, “vertical planes”). The light source in both setups was a Photonics DM30-527-DH Nd:YLF dual-cavity high repetition rate pulsed laser (527 nm, 30 mJ/pulse) with a pulse separation time of 50 μ s for the rotor outflow and 200 μ s for the vertical plane measurements. Adjustable sheet optics with a $f = -20$ mm focal length cylindrical lens were used to generate the laser sheet, resulting in a 10-deg divergence angle and a waist thickness of approximately 2 mm at the landing deck. Seeding particles with a nominal diameter of 4 μ m were generated with a Rosco Vapour fog generator placed upstream in the tunnel settling chamber using the Rosco Fog Fluid (propylene glycol). Figure 6 shows the laser plane illuminating the seeding particles in the vertical plane configuration.

For the rotor outflow measurement configuration, a horizontal laser sheet was used 5 mm ($\approx 0.05R$) below the rotor disk. Two LaVision

**Fig. 7. PIV camera setup for the rotor outflow measurements. (a)** The laser sheet, area of interest, and viewing windows for the cameras on the elevated platform. **(b)** A CX2-25 camera mounted with a Scheimpflug adapter under the platform. **(c)** Right-side camera viewing through the window.

Imager CX2-25 cameras (5296×4584 pixels full resolution, 2.7 μ m pixel size) were mounted below the elevated platform, viewing through a pair of clear acrylic windows on the platform as shown in Fig. 7. The cameras were fitted with 50 mm lenses with an aperture of $f/4.0$. These cameras were chosen for the higher spatial resolution due to the smaller viewing angle needed to avoid the edges of the landing deck blocking the rotor disk. In order to increase the temporal resolution, 2×2 hardware pixel binning was activated on the CX2-25 cameras, resulting in a final image resolution of 2648×2292 pixels with an effective pixel size of 5.4 μ m.

In the vertical plane configuration, shown in Fig. 8, two Phantom v341 and a VEO-E 340L CMOS camera (2560×1600 pixels full resolution, 10 μ m pixel size) from Vision Research were used to capture high-speed time-resolved images. Due to the optical accessibility of the tunnel test section, the cameras were placed inside the test section, which slightly increased the cross-sectional blockage ratio. The cameras were equipped with 50 mm lenses at an aperture of $f/4.0$. A reduced field of view (2560×1060 pixels) was used in this study to extend the data acquisition period that was limited by the camera onboard memory, which in turn captured more revolutions of the rotor while retaining most of the region of interest. The laser and the cameras were controlled and triggered synchronously through a programmable timing unit. Furthermore, the laser sheet optics were mounted on a lateral traverse, and a motorized focus control system was integrated into the camera lenses such that the measurement plane could be easily adjusted laterally between experiments by precalibrating the PIV system at each measurement plane in advance.

Acquired image pairs were processed using the LaVision DaVis 10.2 software. The process started with a background removal algorithm using anisotropic diffusion. It has been shown that this method worked well with unsteady reflections caused by spinning propellers in the image background (Ref. 26). The background-subtracted images were processed using a standard multipass cross-correlation algorithm. A universal outlier detection function with a filter size of 5×5 was used during processing to iteratively detect and remove spurious velocity vectors. Regions that were blocked by the ship, rotor, or with substantial light reflections were masked out and were not used for vector calculations. For the rotor outflow study, the initial interrogation window was 96×96 pixels

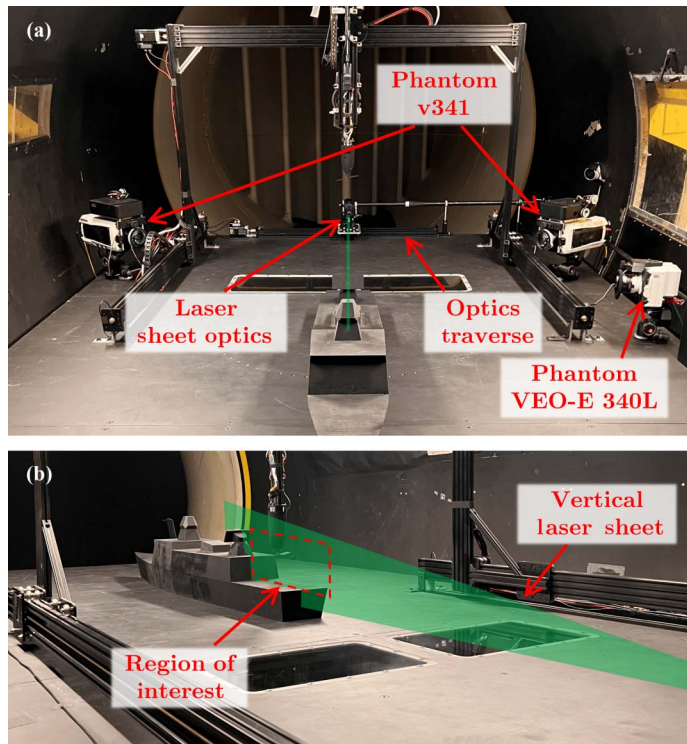


Fig. 8. PIV setup for the vertical plane measurements. (a) Placement of the cameras and optics. (b) Laser sheet orientation and the region of interest.

Table 3. Test matrix of the force and moment survey

Rotor Height Above Deck (h)	WOD Angle (ψ)	Number of Grid Points
$0.92R$ (h_{HOD})	0	45
	G5, R5	45
	G15, R15	45
	G30, R30	42
	G60, R60	40

with 50% overlap, and the final window size was 48×48 pixels with 75% overlap. This resulted in a vector spacing of 1.28 mm. In the vertical plane measurements, the initial window was 64×64 pixels with 50% overlap, and the final window size was 32×32 pixels with 75% overlap. Depending on the position of the laser plane relative to the cameras, the resultant vector spacing ranged from 1.16 to 1.44 mm.

Test matrix and procedure

The test matrix in this study consisted of a stationary rotor force and moment survey across a grid of fixed locations around the landing deck for various WOD angles. Then, a PIV investigation with the two different optical setups discussed previously was conducted for the rotor hovering above the landing deck at different WOD angles. Finally, an attempt to study a dynamically approaching rotor with PIV was performed to gain insight into the transient aerodynamic phenomena that occurred while the rotor entered the influence of the ship airwake and recirculation region close to the hangar wall. All studies were conducted with the concurrent acquisition of surface pressure measurements on the ship deck and hangar wall.

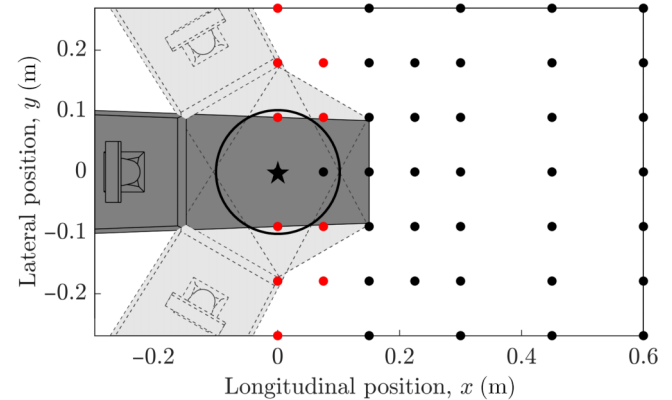


Fig. 9. Grid survey points of the rotor hub behind the ship where red points indicate positions skipped at higher ship WOD angles. (Shaded geometries indicate a 60-deg WOD angle for reference. The star symbol denotes the HOD position. The black circle shows the size of the rotor disk at HOD.)

During the force and moment survey, the position of the rotor hub was moved across a grid of points behind the ship superstructure. Table 3 shows the extent of the survey including ship WOD angles, hovering height, and the number of grid points. Figure 9 illustrates the grid of survey points. Note that the points marked in red were skipped or partially skipped at higher WOD angles due to the structural interference between the rotor disk and ship superstructure.

The ship was manually adjusted to the desired yaw angles for Green (G) or Red (R) wind angles¹ prior to starting each test condition. Before each survey, the rotor was first trimmed to the desired thrust and zero in-plane moments at an up-and-away position at the target wind speed, which minimized the influence of the ship airwake on the rotor trim. Figure 10 illustrates the relative distances between the hover-over-deck (HOD) and up-and-away positions. Table 4 lists the statistics of the trimmed results of rotor hub loads at the up-and-away position for all measurements taken. The rotor trim control was then maintained and fixed throughout the run. Data acquisition of loads and pressures were sampled at 1600 Hz and 800 Hz, respectively, and were triggered simultaneously after a 15-s settling period once the rotor reached each target position. With the limited tunnel entry time, data were acquired for 10 s at each position in order to capture sufficient cycles of the low-frequency content while keeping the duration of the experiment manageable. After each run, the rotor was returned to the up-and-away position and a measurement was taken to ensure data consistency. A total of four survey runs were performed for each test condition to quantify the measurement uncertainties.

A similar procedure was used for the rotor PIV experiments. The rotor was first trimmed in the up-and-away position and brought to the target position while keeping the trim control to the servos constant. Data acquisition was then initiated after a sufficient period of settling time (15 s) when the rotor reached the target position. After each test run, the rotor was again traversed back to the up-and-away position for consistency checks. Table 5 lists the test matrix for the PIV studies. One single horizontal measurement plane located 5 mm below the rotor disk was used for the rotor outflow study with the rotor hovering at the HOD position

¹G, or Green, angles are wind conditions where the relative wind is blowing onto the deck from the starboard side of the ship. R, or Red, angles indicate the wind coming from the port side. For example, a G15 condition means that the freestream comes from a direction that is angled 15 deg to the right of the ship centerline, equivalent to a 15-deg ship yaw relative to the freestream.

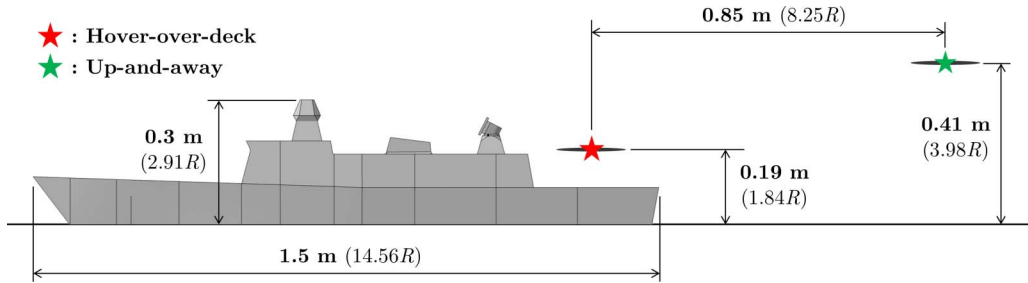


Fig. 10. Relative position of the rotor hover-over-deck and up-and-away positions.

Table 4. Statistics of mean rotor loads and RMS thrust at the trimmed up-and-away condition

	C_{F_x} ($\times 10^{-5}$)	C_{F_y} ($\times 10^{-4}$)	C_T ($\times 10^{-3}$)	C_{M_x} ($\times 10^{-5}$)	C_{M_y} ($\times 10^{-5}$)	C_{M_z} ($\times 10^{-4}$)	T_{rms} (%)
Mean	-9.94	-1.90	5.77	-1.03	1.88	7.86	2.01
Standard deviation	2.84	0.19	0.09	3.57	3.42	0.19	0.25
Minimum–maximum range	16.99	1.10	0.52	20.44	19.78	1.14	1.25

Table 5. Test matrix of the PIV studies

Measurement Configuration	Rotor Position	WOD Angle (ψ)	Number of Planes
Rotor outflow plane (5 mm below the rotor $\approx 0.05R$)	HOD	0	1
		G5, R5	
		G15, R15	
		G30, R30	
		G60, R60	
Vertical planes (20 mm spacing $\approx 0.2R$)	Port starboard	0	13
	HOD	0 G15, R15	
Isolated ship	Port starboard	0	3 ^a
	Isolated ship	0	11
		G5, G15	13
		G30, G60	17

^aOnly three planes were measured with one intersecting the center of the rotor and one on either side of the rotor at approximately 0.6R.

under wind angles of up to 60 deg. Images were obtained at 100 Hz over 10 s, giving a total number of 1000 flow realizations per test that were used for time averaging.

For the vertical plane configuration, a plane spacing of 20 mm ($\approx 0.2R$) was used, giving a total of 13 measurement planes to cover the span of the rotor disk when hovering at the HOD position under headwind and 15-deg wind in both directions. A total of 2000 vector fields sampled at 400 Hz were obtained over 5 s for each test under headwind conditions. In addition, experiments with two laterally offset hovering positions at the port and starboard edges of the landing deck ($y = -0.09$ m and $y = 0.09$ m with $x = 0$ m) were also performed for both the rotor outflow and vertical measurement configurations. Finally, a set of vertical plane measurements with the ship in isolation was conducted with headwind and Green winds of up to 60 deg for baseline reference.

Lastly, an initial investigation of the rotor dynamically approaching the ship was carried out to assess the rotor transient response and the feasibility of the experimental technique. The rotor was commanded to approach the HOD position along a 3-deg linear approach path,

longitudinally in headwind conditions with a constant approach velocity of 0.025 m/s. This approach velocity was geometrically scaled to be equivalent to approximately 5 kt (2.6 m/s) at full scale. This means that the distance covered within a certain time interval was 1/100 of full scale. No dynamic scaling (i.e., scaling through rotor tip speed or advance ratio) was performed due to the limitations of the experimental setup. As the rotor approached the target position, a constant deceleration of 0.025 m/s² was set to bring the rotor to a hover within 1 s. After reaching the HOD position, the rotor was kept in position for 5 s while still continuously taking measurements. Utilizing the same setup as in the vertical PIV measurements, time-correlated data acquisition of rotor loads, pressure, and PIV was conducted. The sampling rate for PIV was reduced to 100 Hz, trading off temporal resolution such that the image acquisition period could be extended to 20 s (the limiter being the camera onboard memory). This covered the majority of the rotor entering the camera field of view, which was focused on the landing deck, and also a 5-s hovering period after the rotor reached the target position to investigate any unsteady rotor wake settling effect.

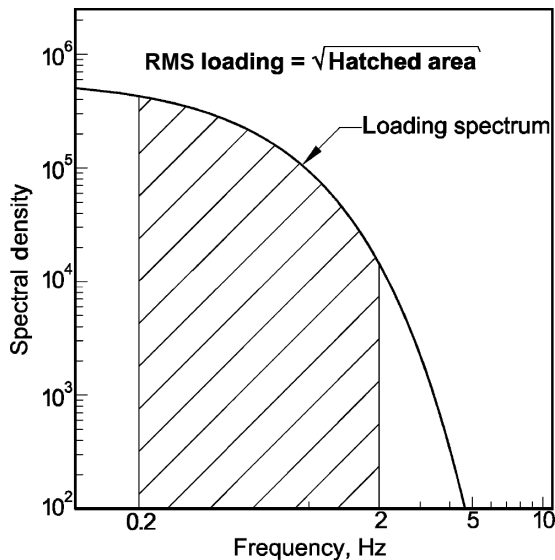


Fig. 11. Definition of the RMS loads (Ref. 1).

Quantification of unsteady rotor loads

In order to relate the measured forces acting on the helicopter to pilot workload, it has previously been shown by McRuer (Ref. 27) and adopted by Lee and Zan (Ref. 2) that the unsteady load components in the 0.2–2 Hz range at full scale, also known as the closed-loop pilot response frequency range, pose a significant challenge to helicopter pilots. This accounts for the fact that higher frequency loads do not affect the handling qualities of the vehicle significantly, and, at the lower frequencies, the pilot can compensate through manual helicopter controls relatively easily. To quantify this unsteadiness, the root-mean-square (RMS) loads were defined by taking the square root of the integral over the power spectral density (PSD) of the time history of loads within the above-mentioned frequency range at full scale, as shown in Fig. 11.

It has been shown experimentally by McTavish et al. (Ref. 3) that there was a positive correlation between the normalized RMS rotor thrust (T_{rms}) in subscale experiments and the full-scale helicopter pilot workload. In subscale experiments, this frequency range was scaled by the ratio between the rotor angular rate of the scaled wind tunnel model and the full-scale reference. The approach was also derived in detail by McTavish et al. (Ref. 3). In this present study, this corresponded to a frequency range of 3.86–38.6 Hz. Additionally, prior to integrating the PSD spectrum, a smoothing spline function was fitted to the frequency range of interest to eliminate known resonance frequency peaks (10–15 Hz) from the rotor traverse and support structure. A similar approach was employed by Fernandez et al. (Ref. 19).

Wind tunnel blockage correction

Due to the substantial blockage effect from the experimental setup, especially when the ship was yawed at higher angles to the freestream, corrections must be made to the dynamic pressure to ensure comparability across test conditions. The reference dynamic pressure in this experiment was measured with a pitot-static probe upstream of the ship model. Since the ship model and traverse system were not aerodynamically shaped, solid and wake blockage corrections were estimated jointly using the relation introduced by Barlow et al. (Ref. 28), where the corrected dynamic pressure (q_c) is shown in Eq. (1) below:

$$q_c = q_u \left(1 + \frac{1}{2} \frac{A_f}{A_t} \right) \quad (1)$$

where q_u is the uncorrected dynamic pressure measured by the pitot-static probe, A_f is the model frontal area, and A_t is the cross-sectional area of an empty tunnel test section. In this study, A_f included the area blockage from the test models and the rotor traverse system. For A_t , the area considered was the cross-sectional area of the test section that was above the elevated ground platform since the velocity was measured in this region. Based on the angle of the ship model, the estimated increase in dynamic pressure ranged from 4.3% to 6.6% with a ship WOD angle of 0–60 deg. This correction was applied to the pressure coefficient and reference velocity calculations throughout this paper.

Results

Rotor positional effect around the ship deck

Figure 12 shows the contour maps of the change in the mean thrust coefficient (ΔC_T) with the rotor hovering at the HOD height (h_{HOD}) above the landing deck compared with that in the up-and-away position under various WOD angles. The overlaid black markers indicate the grid sample points and the star symbols denote the HOD position above the landing deck. In a headwind, one can see that the maximum rotor thrust deficit occurred at the stern of the ship. This local minimum likely resulted from the complicated balance between the increasing influence of the ship airwake on the rotor inflow and the benefit from the ground effect as the rotor approached the landing deck.

In addition, the thrust map indicated a slight asymmetry about the centerline ($y = 0$) of the ship even in a headwind condition. This asymmetry showed that the rotor thrust recovered more rapidly as the rotor was gradually positioned towards the starboard side of the ship as compared to the port side. The rotational direction of the rotor could have contributed to this asymmetry. The advancing side of the rotor encountered the fast-moving freestream much earlier when positioned towards the starboard side of the ship, generating more thrust. On the other hand, the advancing side of the rotor was immersed in the low-energy wake region even when placed towards the other side of the ship, resulting in an opposite effect. A similar trend was also observed in wind tunnel experiments by Zan with a 1:50-scale CPF ship model (Ref. 1). It is worth noting that at positions furthest away from the centerline of the ship, the thrust recovered to a value slightly exceeding that in the up-and-away position. This possibly resulted from the blockage that the ship and traverse system presented, introducing slightly accelerated flow towards the edges of the surveyed area, which resulted in slightly increased translational lift for the rotor.

As the WOD angle increased, the magnitude of the maximum thrust deficit grew due to the escalating disturbances from the separated airwake. At the same time, the low-thrust area shifted towards the region behind the ship superstructure with a greater impact and a widened field of influence. A positive change in thrust was seen on the landing deck for Green winds starting as early as 5 deg and continuously covering a larger portion of the landing deck up to 30 deg compared with Red winds. This finding aligned with the observation discussed earlier, where the thrust recovered more significantly towards the starboard side of the ship in the headwind. However, this trend started to reverse from 30 up to 60 deg.

At 30 deg, although G30 still exhibited greater coverage of positive change in thrust over the deck, the maximum increase within the surveyed region was higher in the R30 case. As the wind angle was increased, the freestream impacted the windward side of the landing deck with a larger angle of incidence, causing a more significant separation over the deck. The updraft caused by this separation could have resulted in a greater “cushioning effect” on the rotor which augmented the thrust generation towards the windward edge of the landing deck. To support this, the vertical velocity contour of the ship in isolation at a WOD angle

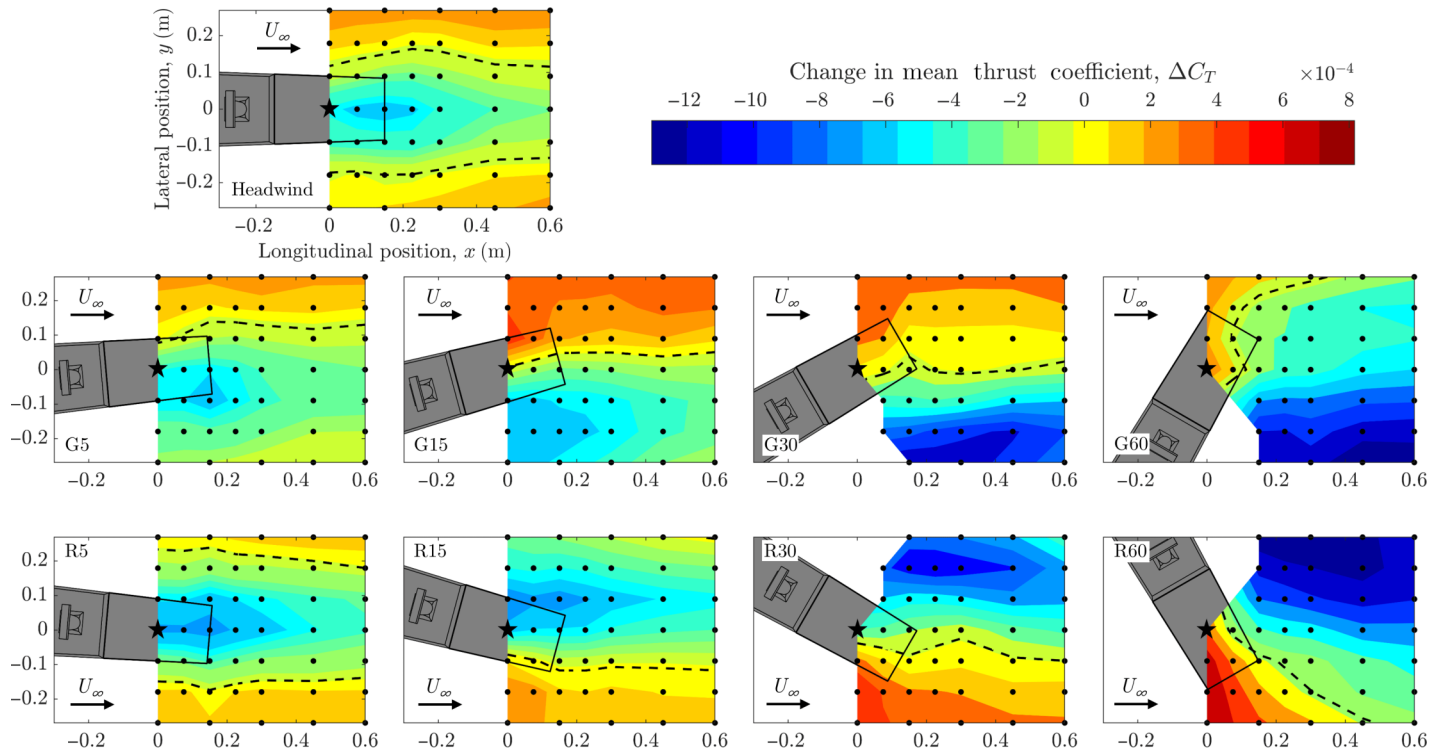


Fig. 12. Change (relative to up-and-away) in mean thrust coefficient around the landing deck at HOD height ($0.92R$) under different WOD angles. (The star symbol denotes the HOD position. Dashed lines indicate zero crossings.)

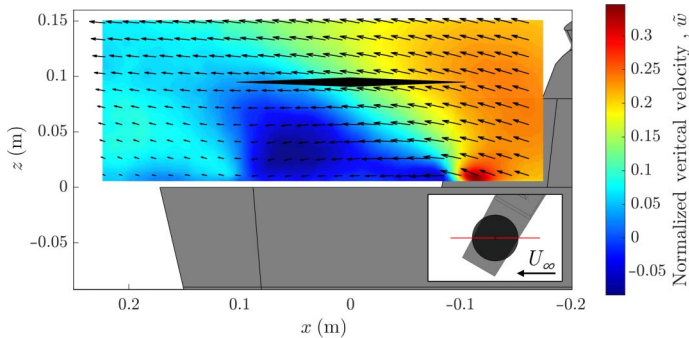


Fig. 13. Time-averaged normalized vertical velocity at $y = 0$ m with the ship in isolation under G60 wind. (The rotor disk, marked in black, was superposed to illustrate its relative position. Every sixth measured vector is shown.)

of G60 is shown in Fig. 13. An illustration of the rotor disk at the HOD position was superposed in the figure to show the relative positions. It was clear that the upwind side of the rotor would be subjected to the updraft from the side walls of the landing deck at high WOD angles. This effect could be seen in winds from both sides of the ship, but the Red winds had a more prominent effect in Fig. 12. This finding suggested that the direction and location of the separated flow interacted with the rotor and had a considerable influence on the rotor thrust at constant rotational speed.

Figure 14 shows the change in the normalized RMS thrust value expressed in percent of mean local thrust compared with the up-and-away condition within the same survey domain discussed previously. It shows that, under a headwind, the location where the ship airwake induced the highest unsteady thrust on the rotor coincided with the location of minimum mean thrust. However, the influence of the ship on the unsteadiness

diminished faster towards the port side of the ship, as the rotor moved away from the centerline, which was an opposite trend than that observed in the change in mean thrust. Again, this was likely due to the ship airwake impinging different regions of the rotor disk. As the rotor was traversed towards the starboard side away from the ship, the retreating side of the rotor disk remained inside the highly unsteady wake region longer than when moving in the opposite direction. The higher RMS thrust towards the starboard side suggests that the ship airwake had a greater unsteady impact on rotor hub loads when interacting with the retreating blade.

As the WOD angle was increased, a shift and strengthening of the region with higher RMS thrust can be seen, similar to that observed in the thrust deficit. Additionally, when comparing the Green and Red winds, the rotor was subjected to higher unsteadiness in thrust towards the windward side of the ship under Green wind conditions. Interestingly, a bifurcation in the highly unsteady region started to emerge downstream of the landing deck when reaching G30, which was not seen in R30 wind condition in Fig. 14. However, this bifurcation appeared to have coalesced into one when reaching G60. The bifurcation was most pronounced under G30 winds where the two high unsteadiness regions approximately aligned with the downstream wake of the radar and superstructure and the flow separation roll-up from the windward side of the landing deck.

To support this observation, a series of turbulent kinetic energy (TKE) contours with the ship in isolation at different WOD angles are shown in Fig. 15. These four cross-plane contours in each wind condition, ranging from $x = -0.1$ m to $x = 0.2$ m separated by 0.1 m, were slices generated through a 3D modified Akima piecewise cubic interpolation method using data from all streamwise measurement planes. This method was chosen to avoid unrealistic overshoots during interpolation. One can see that two noticeable unsteady wake regions started to emerge at different locations and also at different heights downstream of the radar and landing deck under a 15-deg wind. The strength of these two regions grew and

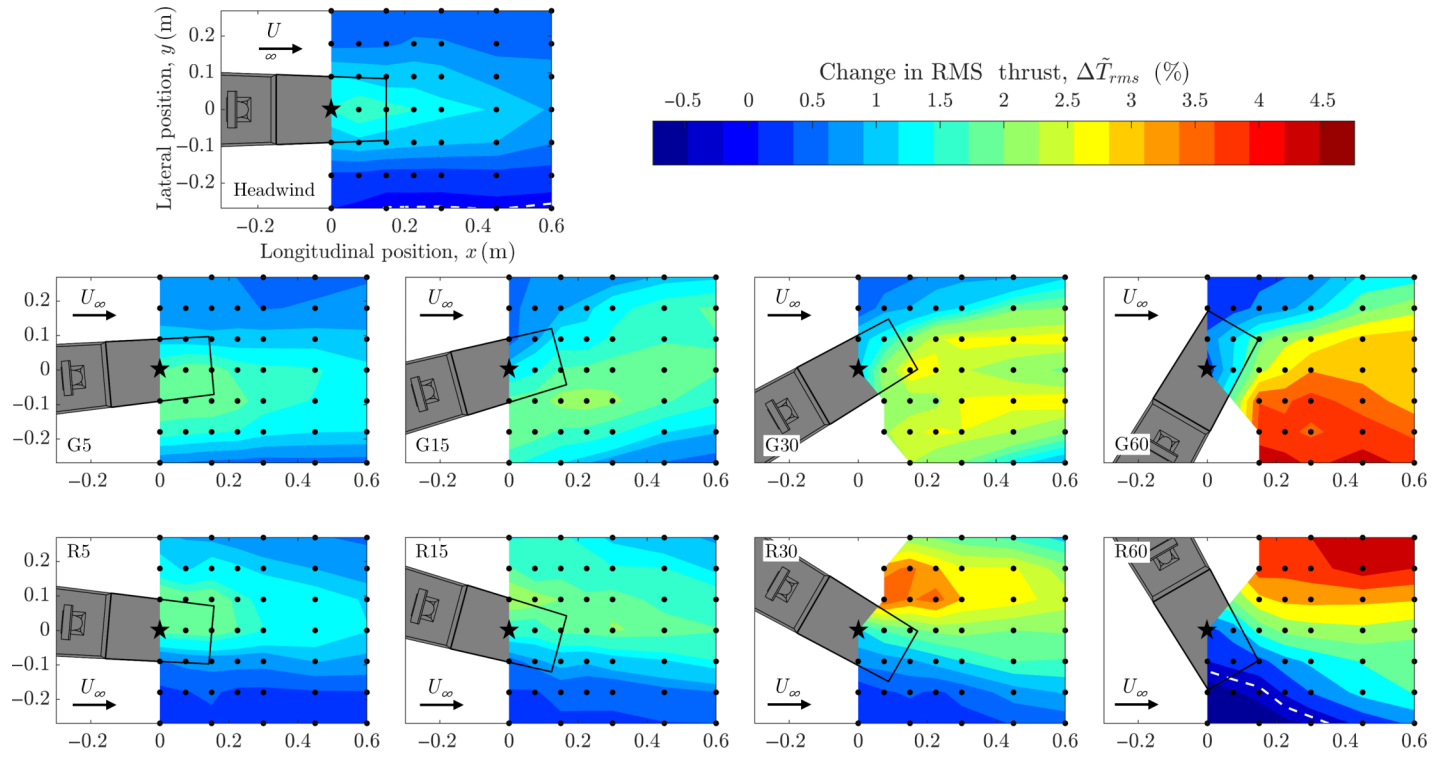


Fig. 14. Change (relative to up-and-away) in unsteady thrust around the landing deck at HOD height (0.92R) under different WOD angles. (The star symbol denotes the HOD position. Dashed lines indicate zero crossings.)

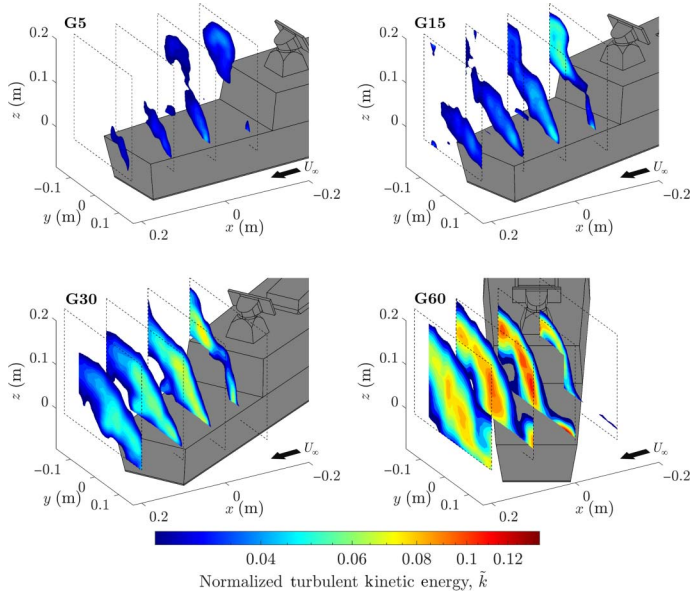


Fig. 15. Contours of normalized TKE at $x = -0.1, 0, 0.1$, and 0.2 m with the ship in isolation under Green winds from 5 to 60 deg. (Low values under 0.025 were cut off and not shown.)

started to merge as the WOD angle was increased to 30 deg. When at 60 deg, the turbulent fluctuations further intensified, and there was no visible distinction between the two regions anymore.

Figure 16 shows the change in unsteady thrust extracted from the $x = 0.6\text{ m}$ line at 30 deg overlaid on top of the ship geometry with the regions of high upstream TKE indicated. One can notice that under a G30 wind, shown in Fig. 16(a), the two peaks in unsteady thrust happened

when the high turbulence regions were on the left, or retreating, side of the rotor disk. Although in the center position, the advancing side of the rotor was under the influence of the wake from the ship deck, the fact that the rotor encountered more undisturbed freestream flow and exited the influence of the radar wake on the retreating side contributed to a dip in thrust unsteadiness. On the other hand, under an R30 wind (Fig. 16(b)), this was not the case. Only one peak was observed and the location was skewed towards the side shadowed by the ship (i.e., higher positive y -values). The fact that the retreating side of the rotor encountered the unsteady regions while the ship-disturbed flow essentially blanketed the entire rotor resulted in the single peak shown in the figure. These differences in location where the ship airwake interacted with the rotor disk possibly resulted in the distinct effect in rotor loads between Green and Red winds.

Regarding the moments exerted on the rotor, Fig. 17 shows the contour map of the change in mean rolling and pitching moment on the rotor under a headwind. For brevity, only the headwind condition will be discussed here. The reported moments here were with respect to the rotor hub with the x -axis pointing upstream and the y -axis towards the right (starboard) side. From Fig. 17(a), the rotor showed a negative pitching moment (pitch-down) when immersed in the ship airwake with the highest pitch-down moment observed to be at the HOD position. This suggests that the airwake from the ship and the recirculation behind the hangar wall had a greater impact on the thrust generation on the forward section of the rotor disk. In Fig. 17(b), the rolling moment exhibited a strong asymmetry while the pitching moment showed a symmetric distribution about the centerline of the ship. The influence of the ship airwake on the rotor induced a noticeable positive rolling moment (roll-right) along the port side edge of the landing deck. This effect was not seen on the starboard side, where the rotor appeared to be relatively balanced in the roll axis (i.e., close to the up-and-away trim condition).

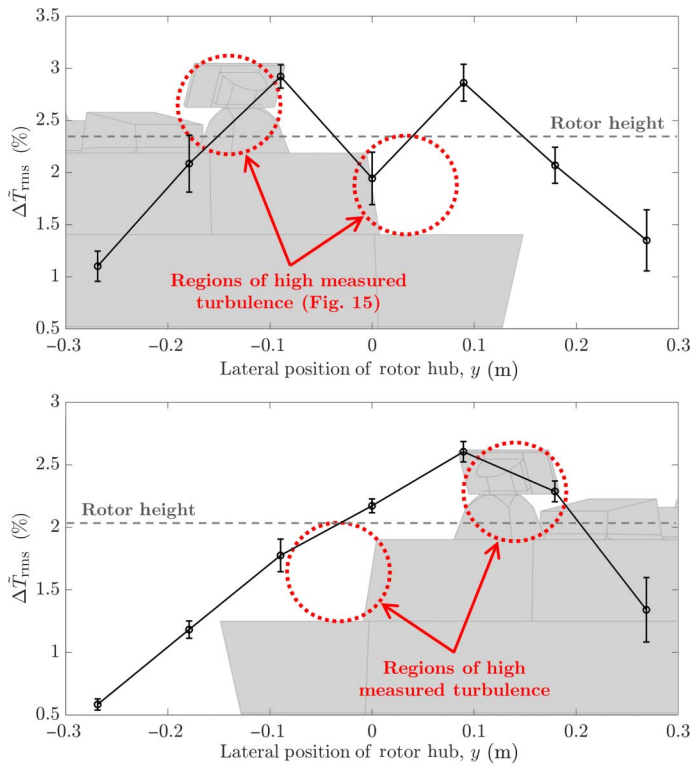


Fig. 16. Lateral profile of the change in normalized unsteady thrust at $x = 0.6$ m for (a) G30 and (b) R30 winds. (Error bars show ± 1 standard deviation (STD). Regions of high measured turbulence in R30 were postulated as a mirrored image of the G30 case.)

To further investigate what caused the distinct phenomena in the moments on the rotor, the velocity distribution in the vertical planes with the rotor hovering on the port side ($y = -0.09$ m) and starboard side ($y = 0.09$ m) of the landing deck, as shown in Figs. 18 and 19, were assessed. From the vertical velocity distribution in Fig. 18, one can see that the center planes of the rotor exhibited nearly identical flow fields under both hover positions (port and starboard). The higher downwash in the aft portion of the rotor supports the pitch-down moment mentioned earlier. However, this could also be partially induced by the rotor ingesting the low-velocity wake region caused by the rotor support structure.

To study the effect of the strong asymmetry in rolling moments, the off-center flow fields (i.e., the advancing and retreating sides of the rotor) in Fig. 18 were first compared. For the outboard portions of the rotor, corresponding to the retreating side of the port hover and the advancing side of the starboard hover, nearly identical flow fields between the two hovering positions were obtained (see Fig. 18). This was true for the inboard portions of the rotor as well. If very close to the rotor disk, this velocity essentially represents the inflow velocity of the rotor, which in turn is directly related to the rotor thrust production. The fact that the flow field was symmetric between the two hovering positions suggests that the imbalance in the roll axis should have a similar magnitude but an opposite effect on either side of the ship. However, this was not the case. This further suggests that other important factors might have a significant contribution to this asymmetry in rolling moments.

From the velocity magnitude contours shown in Fig. 19, one can see that the center plane of the rotor again showed nearly identical flow structures and magnitudes with only minor dissimilarities. However, when it comes to comparing the inboard and outboard sections of the rotor disk, where the rotor encountered freestream asymmetries, there were

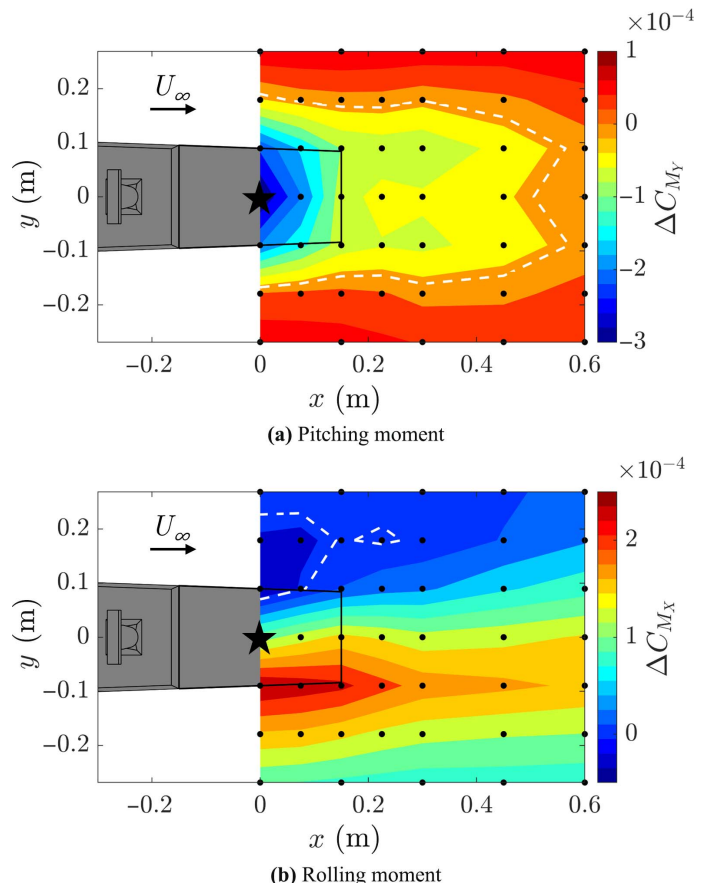


Fig. 17. Change (relative to up-and-away) in mean rotor hub moments around the landing deck at HOD height ($0.92R$) under a headwind condition. (Dashed lines indicate zero crossings.)

noticeable similarities and differences between the two conditions. Overall, both conditions showed higher velocity magnitudes on the retreating side of the rotor compared with the advancing side. This likely resulted from the rotational direction of the rotor. On the advancing side, the rotor-induced swirl was in a direction that opposed the incoming freestream, resulting in a lower velocity magnitude. On the retreating side, the swirl velocity was in line with the freestream, adding up to a higher resultant velocity. This effect was most pronounced under the port hover condition, where the velocity gradient caused by the high-velocity freestream and low-velocity ship airwake was supportive of the rotor swirl.

The fact that the outer portion of the rotor under a port hover had a higher velocity magnitude, or equivalently, a higher mass flow rate across the rotor disk than that under a starboard hover could explain why there was a significant imbalance in roll when hovering on the port side but not on the starboard side. However, caution must be exercised because this postulation relies on simple momentum theory and might not be entirely true under the influence of the ship airwake and landing deck in close proximity to the rotor, inducing unsteady and 3D flow effects that violate the momentum theory assumptions.

To better assess how the ship airwake actually altered the rotor hub loads, the rotor inflow angle was estimated using the rotor outflow PIV measurements. Assuming the rotor outflow PIV measurement plane was sufficiently close to the rotor disk, such that the in-plane wake structure had not evolved considerably, one could assume that the in-plane topology of the rotor wake measured through PIV approximated that at the rotor disk. However, since the measurement was taken below the rotor

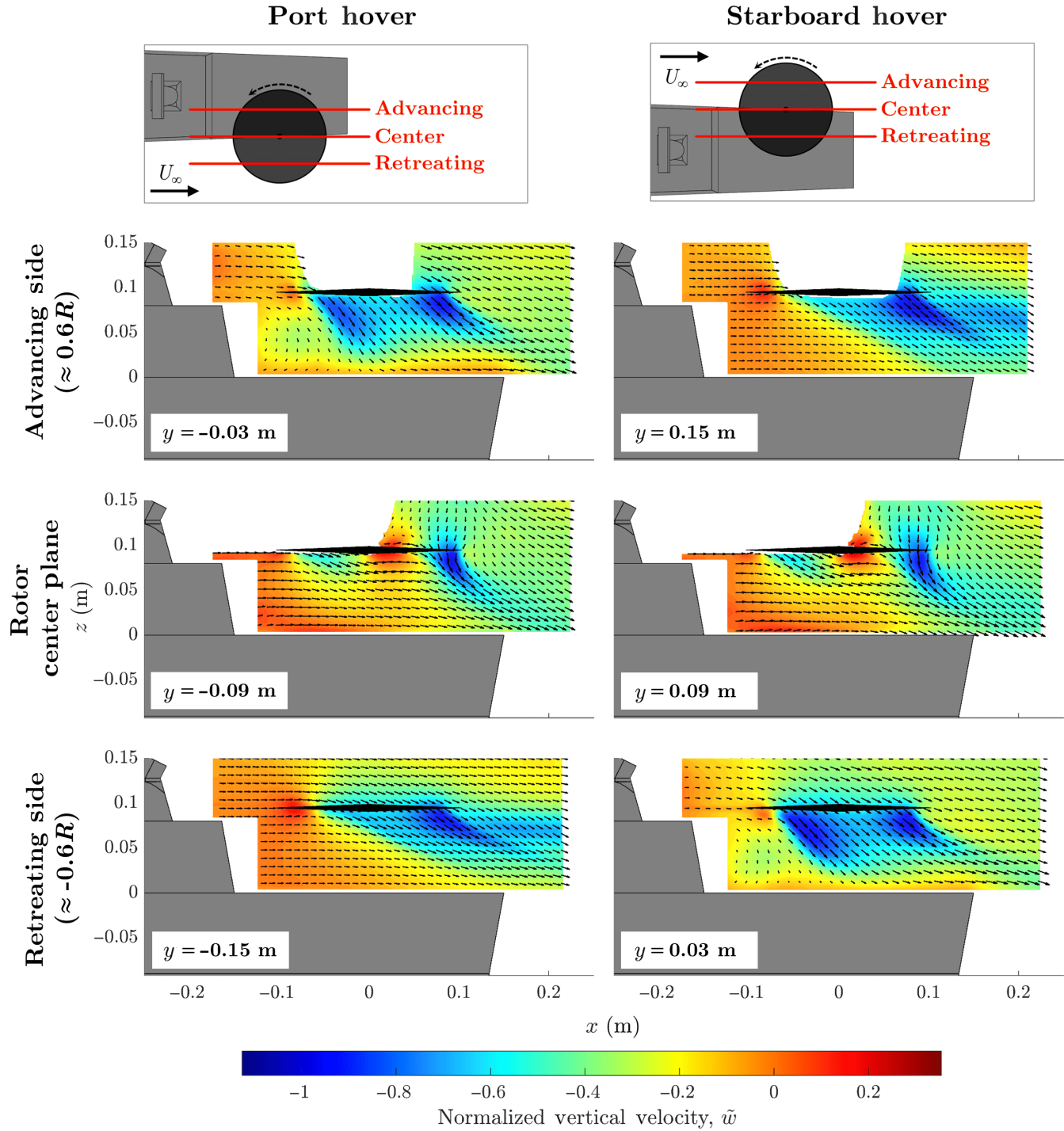


Fig. 18. Time-averaged normalized vertical velocity in the vertical planes at the center, advancing, and retreating side of the rotor hovering at the port and starboard side of the landing deck under headwind. (Rotor indicated in black. Every eighth measured vector is shown.)

disk, the entire wake structure would have shifted downstream due to its convective nature. In order to correct for this shift, a fixed-wake convection model based on Taylor's hypothesis (Ref. 29) was applied here. A similar approach was also employed by Deng et al. to reconstruct a 3D spatial-temporal wake topology of a flapping-wing micro air vehicle through a single measurement plane (Ref. 30).

In this present study, the in-plane topology of the rotor wake was assumed to be "frozen" as soon as it left the rotor disk and translated downstream at a uniform velocity within a short-enough distance. However,

the rotor wake was not only convected downstream in the streamwise direction but also downwards vertically due to the downwash velocity. Thus, the streamwise shift was predicted by first estimating the time it took for the "frozen wake" to reach the measurement plane based on the mean downwash velocity (\bar{w}) within the rotor disk area and the distance between the rotor disk and the measurement plane, which was 5 mm. This time was then multiplied by the mean streamwise velocity (\bar{u}) within the entire measurement domain to obtain the estimated streamwise shift of the wake. Since the shift of the wake was initially unknown, an

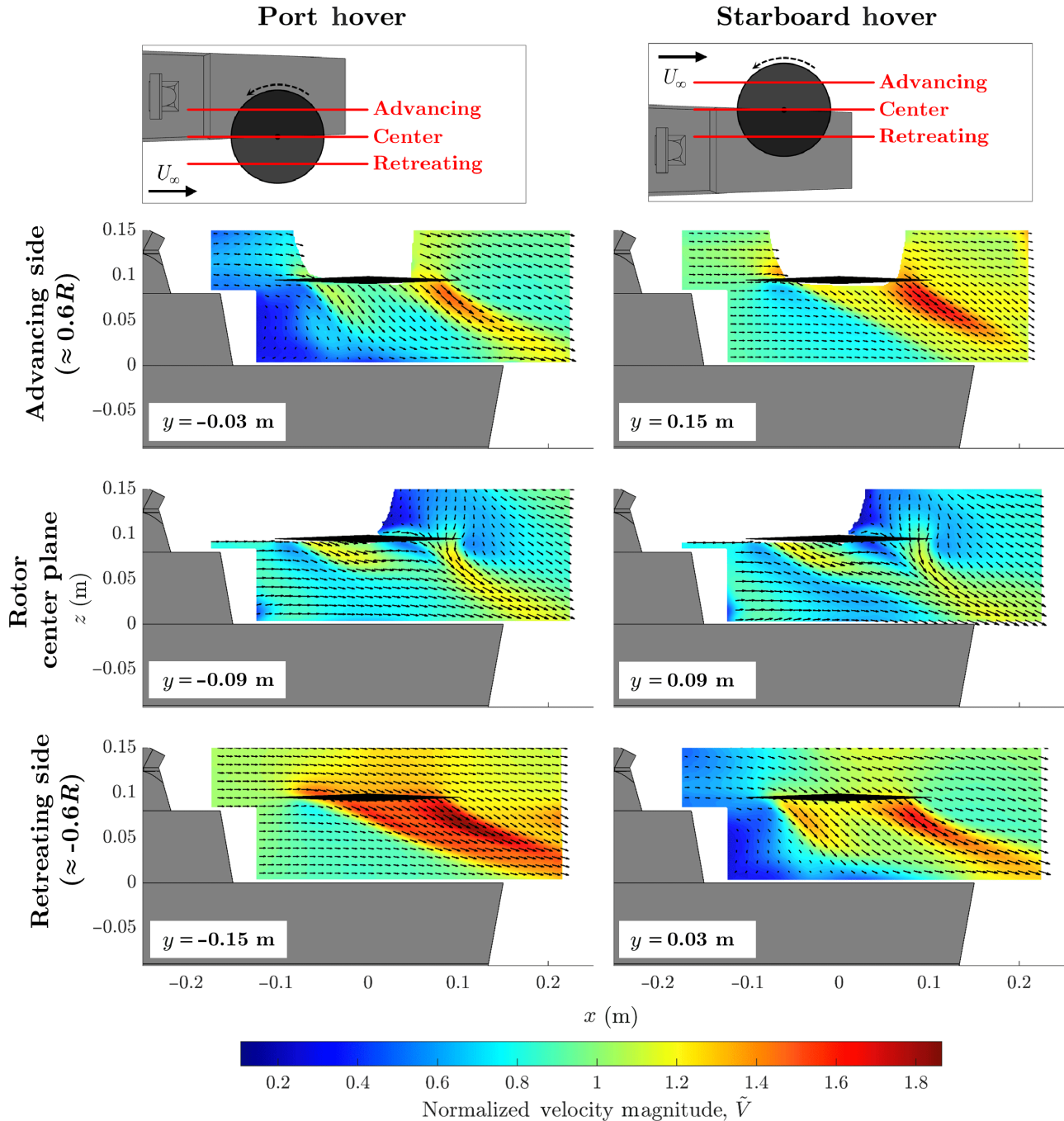


Fig. 19. Time-averaged normalized velocity magnitude in the vertical planes at the center, advancing, and retreating side of the rotor hovering at the port and starboard side of the landing deck under headwind. (Rotor indicated in black. Every eighth measured vector is shown.)

iterative process was used to update the estimation until the shift distance was converged within 0.1 mm. It was found that this process was usually completed within five iterations and the streamwise shift distance was in the range of 6–12 mm, depending on the condition.

After accounting for the wake shift, the rotor inflow angle (ϕ) was calculated by Eq. (2):

$$\phi = \tan^{-1} \left(\frac{U_P}{U_T} \right) \quad (2)$$

where U_P is the normal velocity component through the rotor disk. In this case, it was essentially $-w$ from the PIV measurements. U_T is the

in-plane tangential component that the rotor blades encountered, which was calculated using Eq. (3) below:

$$U_T = \Omega r + (u \sin \Psi - v \cos \Psi) \quad (3)$$

where Ω is the rotor angular velocity, r is the radial location on the rotor disk, Ψ is the rotor azimuth angle, and u, v are the in-plane velocity components obtained from PIV.

Figure 20 shows the inflow angle distributions of the rotor hovering at the HOD position and also laterally offset to the starboard and port edges of the landing deck. Across all conditions, the retreating side of the rotor showed an overall higher inflow angle than the advancing side.

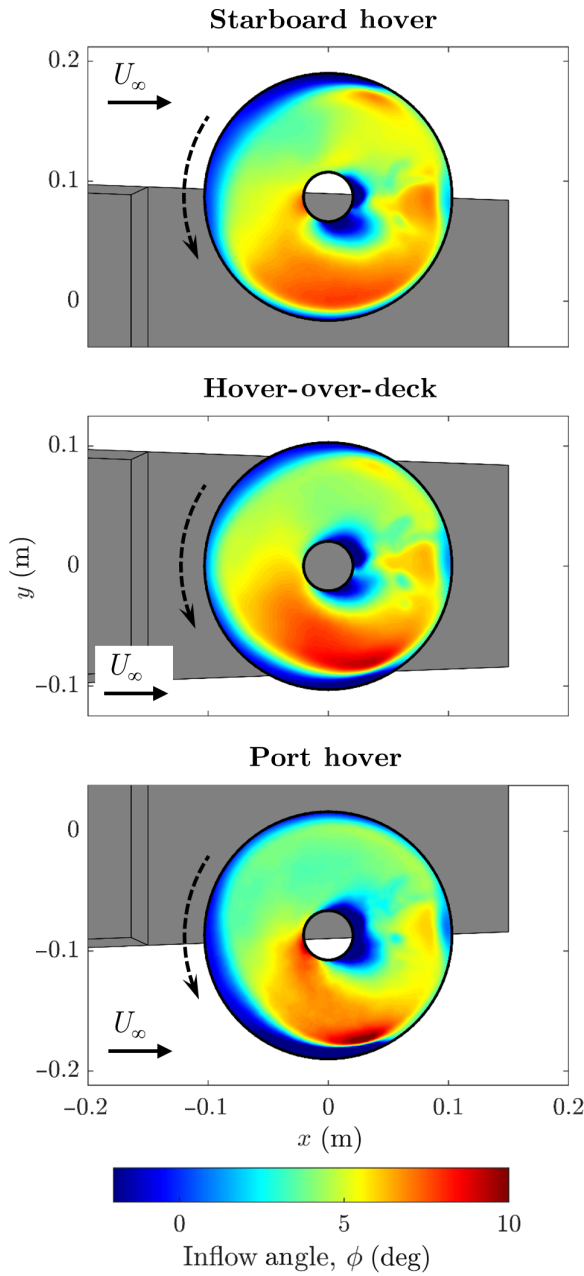


Fig. 20. Time-averaged rotor disk inflow angle distribution with rotor hovering at the HOD position, starboard, and port edges of the landing deck. (Data inside the root cut out, $r < 0.2$, was not shown.)

Note that, apart from the center upwash region caused by the rotor root cut out, the regions further downstream of the rotor hub had a distinct feature that was likely due to the disturbance from the wake of the rotor support structure; see Fig. 5. Additionally, the light reflection off the rotor hub assembly in the background during the experiments could have also lightly affected the results in this region.

In the two edge-hovering cases, the outboard sides of the rotor experienced a significant upwash, indicated by negative inflow angles, at the upwind edge of the rotor disk, which was expected during forward flight. However, due to the low-velocity ship airwake and the proximity to the hangar wall recirculation region, this upwash was hardly visible on the inboard sides of the rotor disk in both cases. This asymmetry in the upwash region most likely contributed to the higher positive rolling moment (roll-right) under a port hover condition. Furthermore, at the

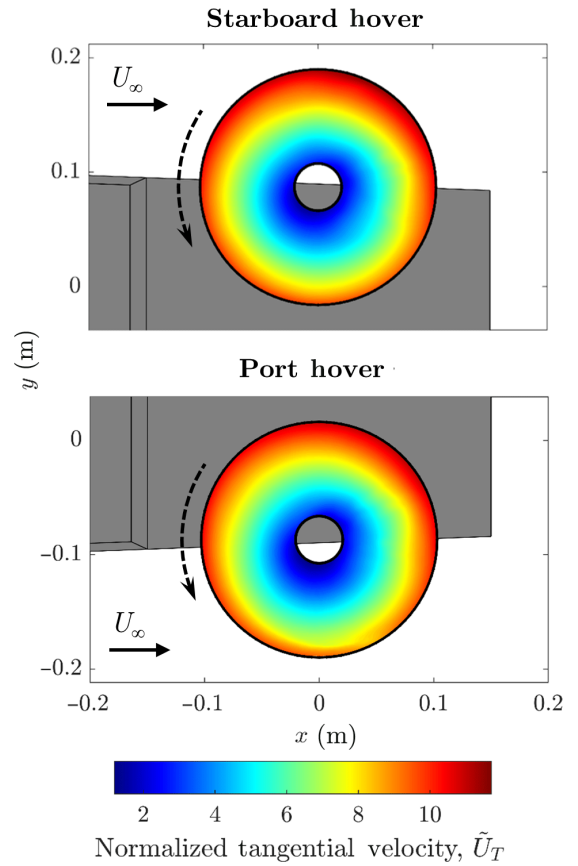


Fig. 21. Time-averaged normalized tangential velocity with the rotor hovering at the starboard and port side edges of the landing deck. (Data inside the root cut out, $r < 0.2$, was not shown.)

HOD position, there was no upwash seen where the rotor disk was closest to the hangar wall. This clearly shows that the additional downwash induced by the ship superstructure airwake and recirculation caused a significant reduction in thrust on the forward half of the rotor disk, subjecting the rotor to a large pitch-down moment, as discussed previously in Fig. 17(a).

Additionally, by simply analyzing the flow that the rotor blade encountered under the influence of the ship airwake, one will realize the ship airwake had a clear asymmetric impact on the rolling moments between the two laterally offset positions. Figure 21 shows the normalized tangential velocities of the two laterally offset hover positions. When the rotor was in a starboard hover, the retreating side was immersed in the low-velocity ship airwake. As a result, a higher relative wind velocity was experienced by the retreating blade, as one can see by comparing the retreating side between the two conditions in Fig. 21. This would increase the thrust on the retreating side, creating a positive rolling moment. However, this was likely counteracted by an opposing moment from the downwash of the recirculation behind the hangar wall, reducing thrust also on the left half (i.e., retreating side) of the rotor. Assuming the advancing side of the rotor was under a similar operating condition as in the trimmed up-and-away position, the rotor would result in a near-neutral rolling moment, seen in Fig. 17(b), if the two opposing effects were of similar strength even when half of the rotor was immersed in the ship airwake.

On the other hand, when the rotor was hovering on the port side, the advancing side was affected by the ship airwake. From the perspective of the advancing blade, a slower velocity was seen, which can also

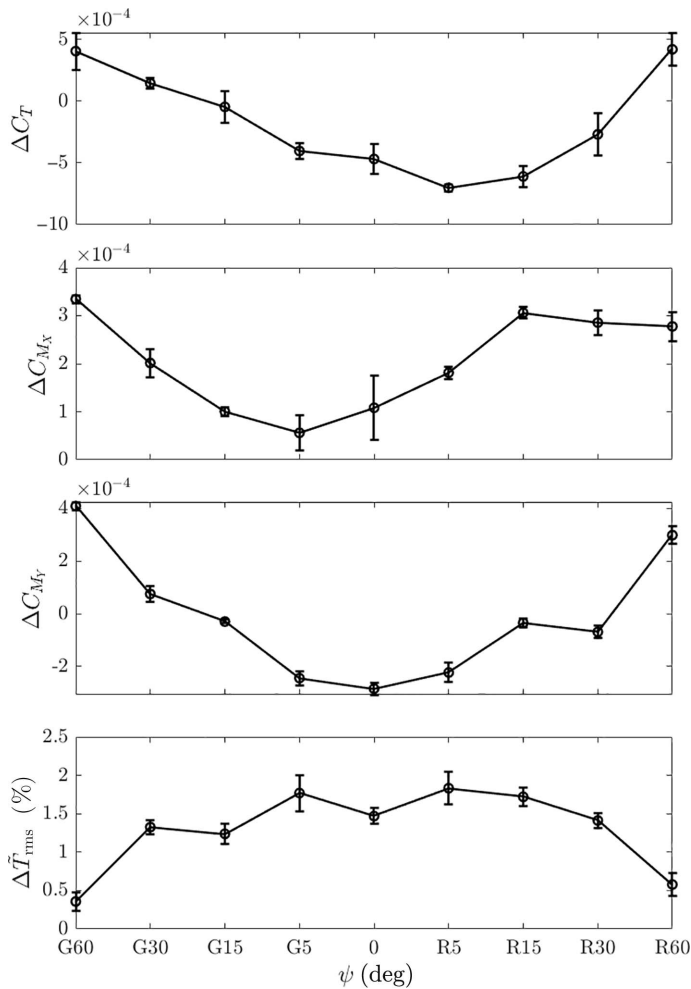


Fig. 22. Change (relative to up-and-away) in thrust, moments, and RMS thrust at the HOD position under different WOD angles. (Error bars show ± 1 STD.)

be observed in Fig. 21. This resulted in less thrust on the advancing side of the rotor, causing a roll-right moment. However, in contrast to the starboard hover, the recirculation region now affects the advancing side of the rotor, also creating a right-rolling moment. Again, now assuming the retreating side was under a similar undisturbed operating condition as in the trimmed up-and-away position, the combination of these effects induced a high positive roll-right moment when hovering on the port side.

WOD angle effect with the rotor at HOD

The rotor at the HOD position was assessed to determine the effect of the WOD angle on the rotor hub loads, flow field, and deck pressure. Figure 22 shows the thrust and moment characteristics of the rotor as the WOD angle was changed. Note that the reference axes for the reported moments had the origin at the rotor hub, the x -axis pointing upstream, and the y -axis towards the right (starboard) side, irrespective of the wind angles. It can be seen that the change in thrust (C_T) was not symmetric about the 0-deg wind angle, but rather skewed with a minimum occurring under R5 wind. The rolling moment (C_{M_X}) also exhibited an asymmetry while the pitching moment (C_{M_Y}) and RMS thrust essentially showed a symmetric variation between Green and Red winds. The rolling moment showed continuous growth in magnitude when increasing the WOD

angle in the Red direction up to 15 deg, but exhibited first a dip and then an increase when going in the Green direction.

The pitching moment showed a very similar trend along the $x = 0$ m line in Fig. 17(a), where a pitch-down moment was present under the direct influence of the ship airwake. When the WOD angle was increased, the disturbance from the airwake reduced as if the rotor was moving away from the centerline of the ship. However, instead of reaching a near-zero pitching moment at the extremities along the $x = 0$ m line in Fig. 17(a), the pitching moment exceeded zero and exhibited a considerable positive pitch-up moment in this case. As discussed previously, the updraft from the freestream impinging the side of the landing deck (Fig. 13) could have resulted in a cushioning effect, similar to a partial ground effect, which partially affected the upwind half of the rotor disk, causing a pronounced imbalance in rotor thrust distribution about the pitch axis. Further experiments exploring these extreme cases will be conducted to answer these questions.

Regarding the RMS thrust, small fluctuations can be seen under Green winds, which most likely resulted from the competing effect of the unsteady ship airwake impacting the retreating side and the freestream impinging on the advancing side of the rotor with different strengths and at different locations. In general, the RMS thrust reduced as the WOD angle increased. Since the RMS thrust was normalized by the local mean thrust value, the higher thrust generated by the rotor at high WOD angles likely resulted in this reduction in RMS thrust.

From the landing deck pressure distributions shown in Fig. 23, the strength and interactions of the disturbed rotor wake with the ship surface can be assessed. Under a headwind, the high-pressure zone under the rotor disk was clearly visible with a peak under the upwind (forward) half of the rotor. A slight asymmetry can also be seen in the contour on the landing deck due to the imbalance in loads from the influence of the ship airwake. This can also be seen in the velocity field shown in Fig. 24, where a dissimilar effect on the advancing and retreating sides of the rotor resulted in different strengths and skew angles in the rotor wake even under a headwind. On the advancing side, the low-velocity ship airwake recirculation region extended further downstream and under the rotor, causing the deck pressure to exhibit a delayed and elongated high-pressure region on the starboard side. On the other hand, on the retreating side, the flow field indicated a smaller recirculation region behind the hangar wall and also a higher rotor wake velocity compared with the other side.

As the WOD angle was increased, in both Green and Red directions, the freestream blowing over and separating from the windward side of the landing deck resulted in a low-pressure region gradually creeping onto the deck, which can be seen in Fig. 23. However, it is worth noting that a clear distinction in pressure magnitude between Green and Red winds started to appear. It is obvious that the pressures on the landing deck, due to rotor wake impingement under Green winds, were significantly higher than those under Red winds from 5 deg up to 30 deg. This phenomenon matches the observation in the change in rotor thrust from Fig. 22, where the thrust values were constantly higher under Green winds from a WOD angle of 5 deg up to 30 deg.

When reaching 60 deg, the difference in pressure distributions between the two wind directions diminished and became essentially a mirrored image of each other. This recovery of symmetry in ship deck pressure distribution supports the fact that the rotor thrust recovered to a similar magnitude at 60-deg winds under both wind directions, as seen in Fig. 22. Furthermore, a significant low-pressure region under both 60-deg wind directions can be seen from the separation at the windward edge of the landing deck. This region of extremely low pressure again suggests that a separated flow from the edge of the landing deck likely resulted in a cushioning effect, even while hovering at the center of the landing deck, creating a net pitch-up hub moment on the rotor.

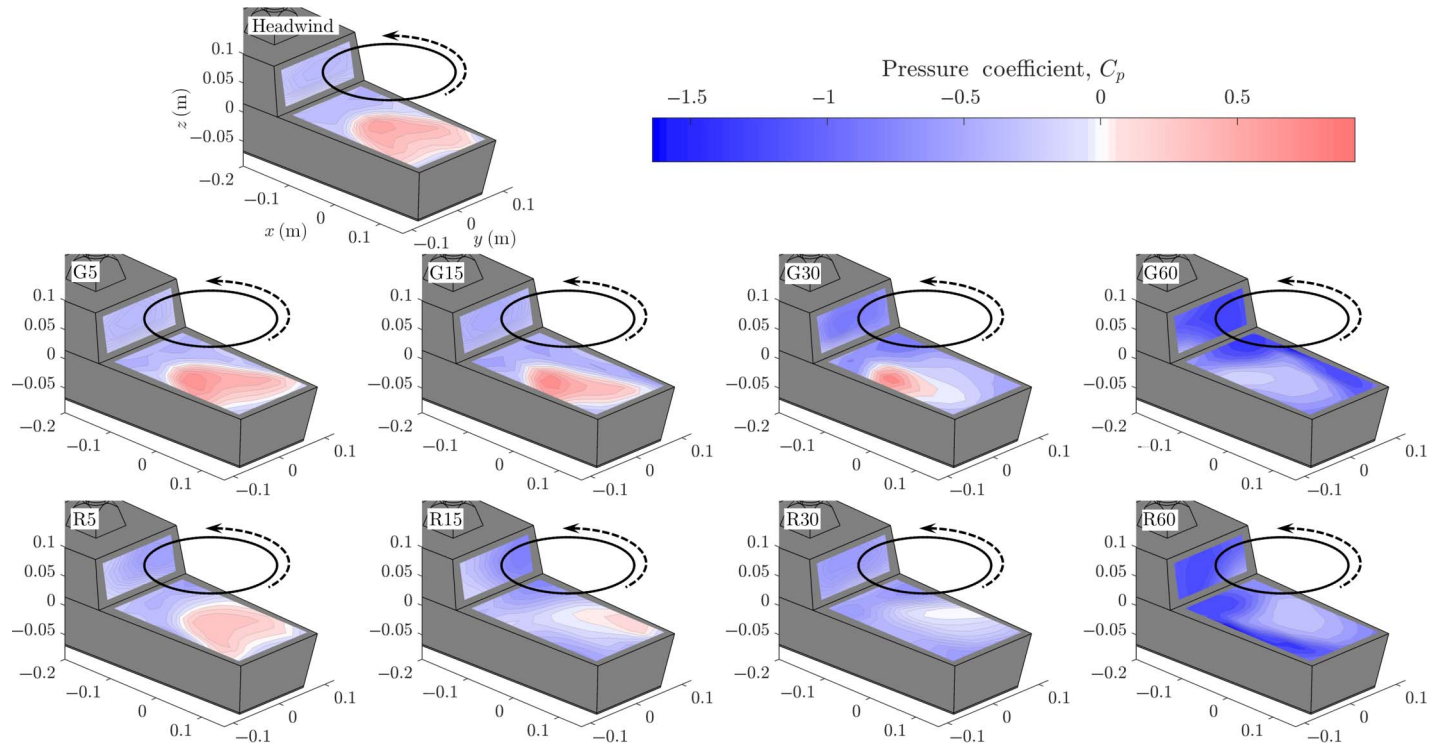


Fig. 23. Time-averaged pressure coefficient with the rotor at HOD under different WOD angles. (The rotor disk is indicated by black ellipses.)

When considering the rolling moments, information could be deduced from the velocity magnitudes shown in Fig. 24. Under conditions shown in the figure, the rotor wake velocities were again greater on the retreating side of the rotor for all wind directions, hence likely contributing to the positive roll-right moments seen across all wind angles in Fig. 22. Furthermore, G15 showed the least imbalance in flow velocity about the roll axis. This was similar to the starboard hover condition discussed earlier where the advancing side of the rotor encountered more undisturbed freestream. On the other hand, the R15 condition had the retreating side of the rotor subjected to the fast freestream, hence the greater combined velocity and possibly resulted in a more significant positive rolling moment shown in Fig. 22.

Again, the above reasoning, which was based on observations of wake velocities, relies on momentum theory. This might not be applicable under the influence of the ship. Thus, by using Eq. (2) and the same procedure described above, the inflow angle distribution within the rotor disk was analyzed to understand the impact on rotor inflow by different WOD angles; see Fig. 25. The upwash region at the windward edge of the rotor disk gradually grew in size as the WOD angle was increased. Based on the wind direction, this region was most pronounced on the sides where the fast-moving freestream impinged on the rotor. This result suggests that the trend in the rolling moment was in the opposite direction as the WOD angle was increased in different directions. However, for larger WOD angles, the trend reversed, as previously seen in Fig. 22. Therefore, it is useful to see exactly how the inflow angle distribution changed under different WOD angles by subtracting the headwind distribution from the distributions under all other WOD angles. The resultant change in inflow angle over the headwind condition is shown in Fig. 26.

Figure 26 shows that there were noticeable magnitude and location variations of the change in inflow angle along the perimeter of the rotor disk as the WOD was changed. For 5 deg, both Green and Red winds showed a decrease in inflow angle on the windward side of the rotor. However, this region under Green wind was concentrated towards the

rotor centerline while the Red wind case was distributed more across the retreating side of the rotor. In addition, the retreating side of the Green wind case showed a noticeable band of increased inflow angle, inducing a left-rolling (towards port) tendency, which was not as visible under a Red wind condition. These observations supported the fact that the rolling moment decreased under G5 wind but increased under R5 wind.

As the WOD angle was increased to 15 deg, the strength of the band of increased inflow angle seen at G5 was significantly reduced. At the same time, the upwash region, while remaining of similar strength, extended further towards the advancing side of the rotor. The overall effect of the decrease in inflow angle on the retreating side was likely greater than the increase in upwash on the advancing side, resulting in a slight increase in the rolling moment. Additionally, the more widespread upwash at the windward edge contributed to a further increase in the pitch-up moment. On the other hand, under R15 wind, the upwash region on the retreating side strengthened and expanded more significantly than that under a Green wind, resulting in both a significant increase in rolling and pitching moment, shown in Fig. 22.

When the WOD reached 30 deg, although the rotor encountered more of the freestream, there was no significant increase in the upwash region on the advancing side under G30 wind. However, on the retreating side, a slight increase in additional downwash on the windward edge was seen with also an appreciable increase in upwash on the leeward edge. Additionally, a small region of increased inflow angle was observed on the leeward edge of the advancing side, which could have slightly reduced the local thrust in that area. The combined effect resulted in a further increase in the rolling moment towards the right. When the rotor was in R30 wind, a slight increase in the windward upwash region on the retreating side can be seen. Additionally, a pair of regions with increased and decreased inflow angles of similar strength and size were present on opposite sides of the rear half of the rotor disk. This induced a roll-left moment that was likely counteracted by the increased upwash on the retreating side mentioned earlier, resulting in almost no change in the net rolling moment compared with the R15 wind condition.

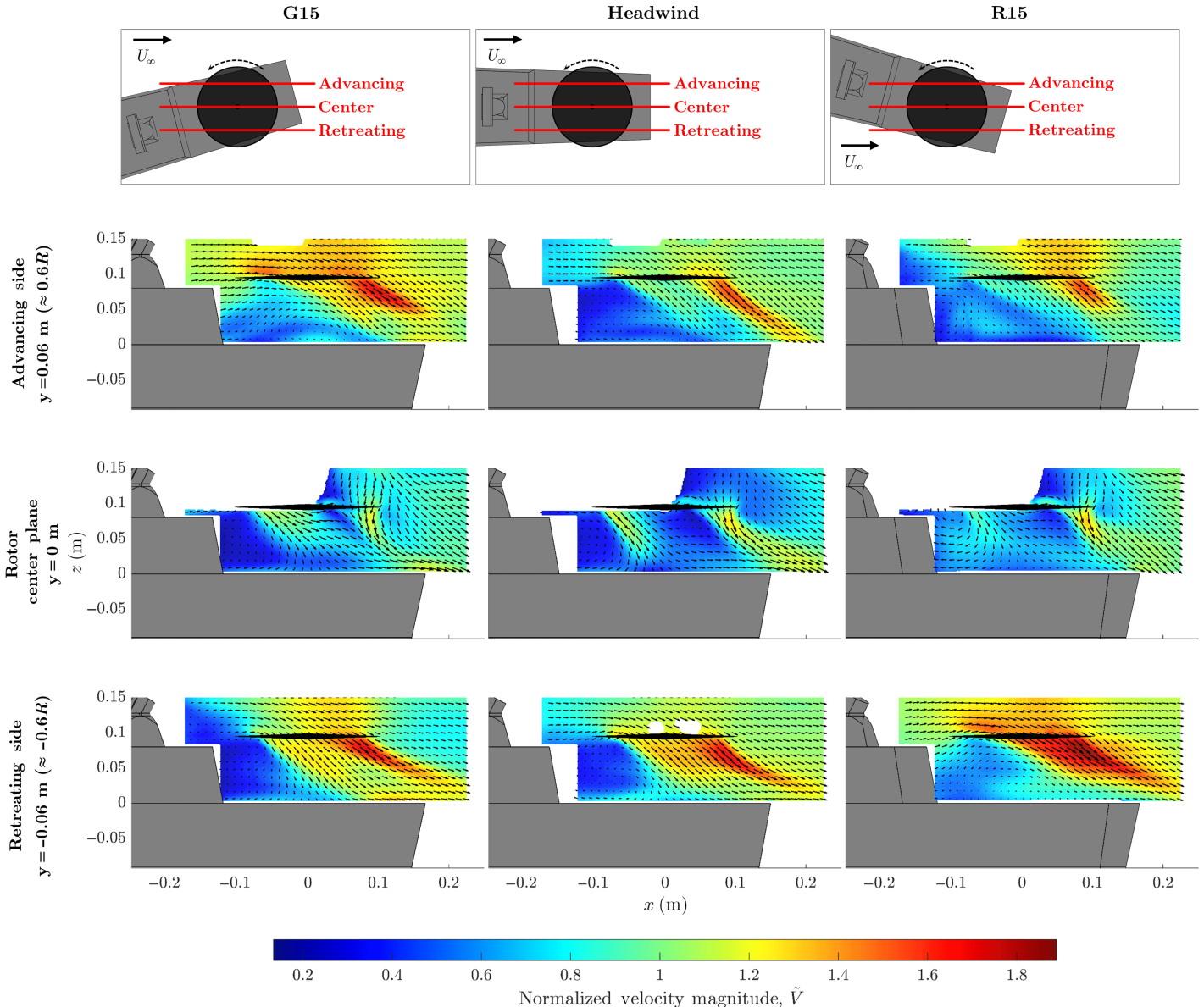


Fig. 24. Time-averaged normalized velocity magnitude in the vertical planes at the centerline, advancing, and retreating side of the rotor hovering at HOD under headwind, G15, and R15 winds. (The rotor is indicated in black. Every eighth measured vector is shown.)

For a WOD angle of 60 deg, a significant area of upwash on the upwind side was observed in both wind directions (Green and Red), suggesting a strong cushioning effect from the separating flow off the windward face of the landing deck that increased the rotor thrust and pitch-up moment. In G60 wind, the windward upwash region further extended into the retreating side of the rotor, and the downwash region on the same side diminished compared with the G30 condition. This resulted in a further increase in the rolling moment towards the right. Since the airwake from the ship superstructure was mostly out of the way of the rotor, the high similarity in the inflow angles between the two wind directions reflected the fact that the rotor hub loads were nearly identical when under a 60-deg WOD angle from both directions; see Fig. 22.

Dynamically approaching rotor

A dynamic experiment of an approaching rotor was conducted to assess the transient response as the rotor approached the landing deck of

the ship. The rotor was brought in at a constant approach velocity (V_{app}) of 0.025 m/s along a 3-deg approach trajectory towards the HOD position under a headwind condition. Figure 27 shows the change in rotor hub loads of a single run along the approach path compared with the up and away measurements. To better observe the change in these measurements, all the time histories of rotor hub loads were fitted with a smoothing spline function to eliminate large fluctuations from sources such as inertial vibrations. Note that after the rotor had reached the HOD position, the rotor was held in hover for 5 s in order to capture the transients. Thus, the curves in the shaded area are time histories of the measurements after reaching the HOD position, and the reader should refer to the time (t) axis labeled on top of the graph. The portion of the curves that are not shaded corresponds with the longitudinal location downstream of the HOD position (x) as labeled on the x -axis.

From Fig. 27, the most fluctuating load component along the approach path was the rolling moment, which, as discussed earlier with Figs. 17(b) and 22, had a strong dependency on the location at which

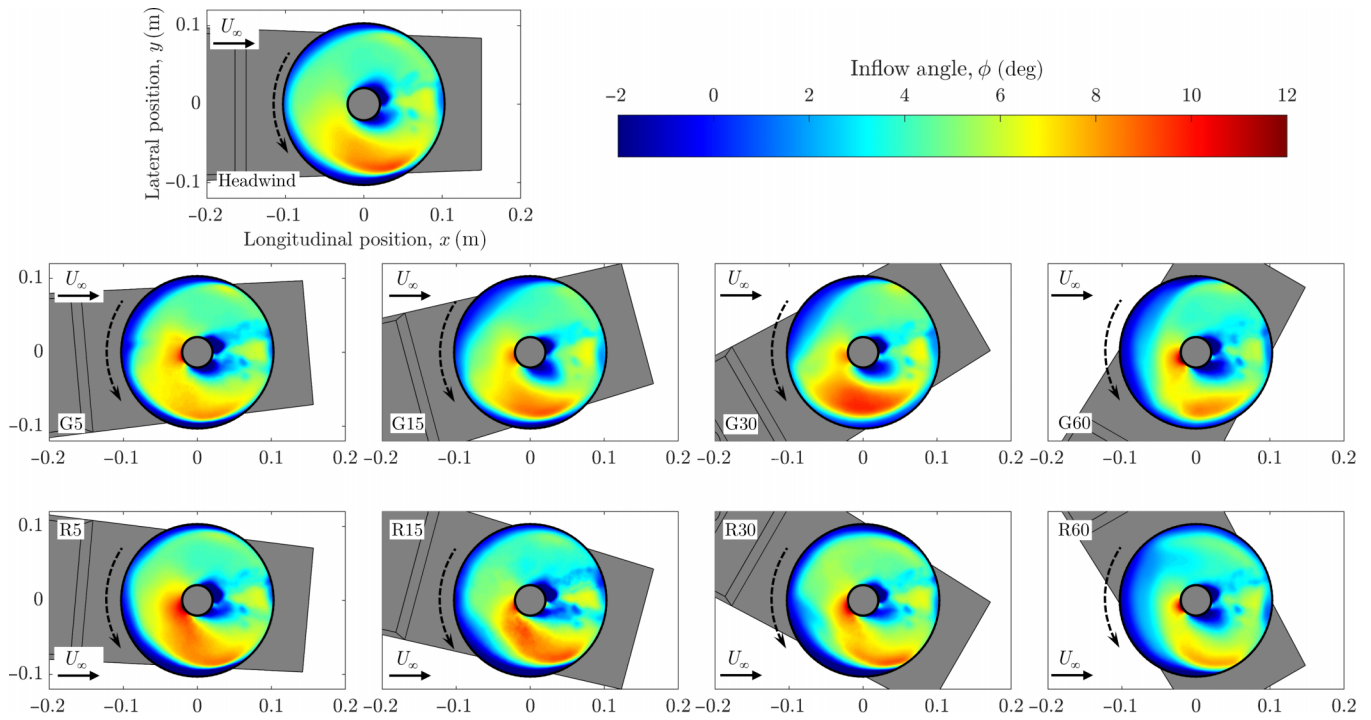


Fig. 25. Time-averaged rotor disk inflow angle distribution with the rotor hovering at the HOD position under different WOD angles.

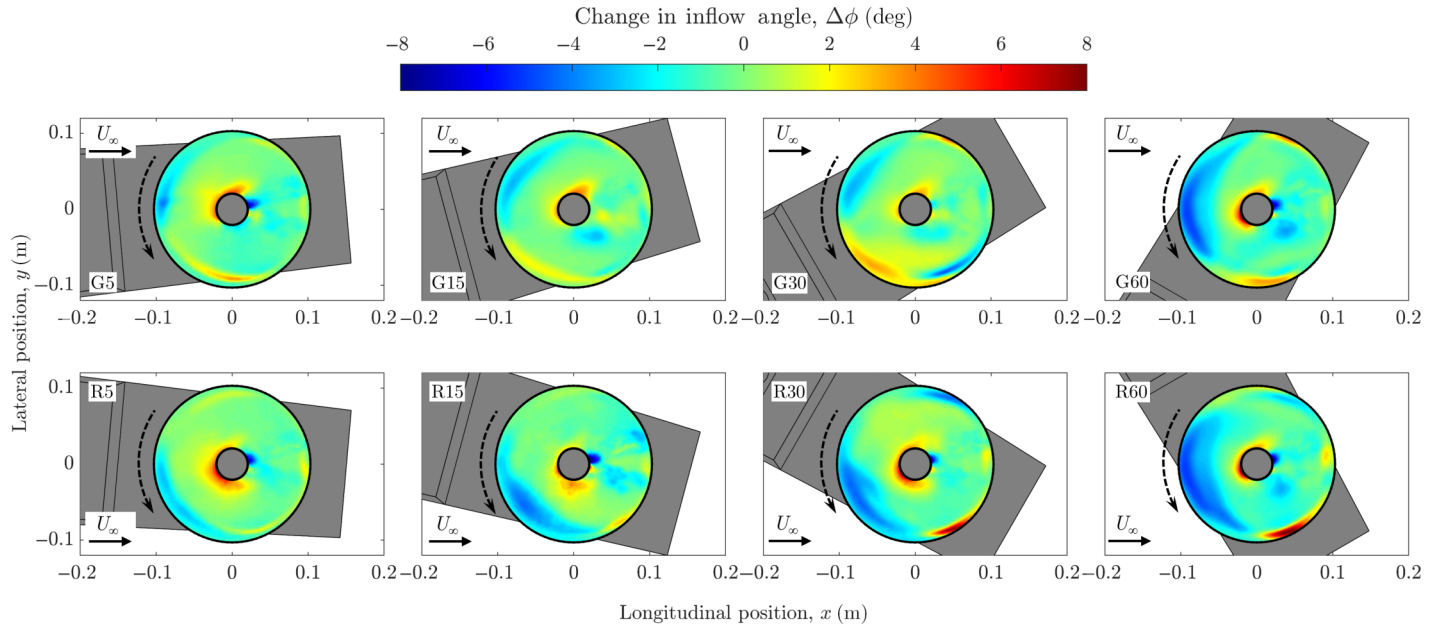


Fig. 26. Time-averaged difference in rotor disk inflow angle distribution between quartering winds and the headwind condition with the rotor hovering at the HOD position.

the ship airwake impacted the rotor disk. The evolution and length scales of the wake structures downstream of the radar and superstructure most likely contributed to these large fluctuations. On the other hand, both the thrust and pitching moment exhibited little change during the early stages of the approach. As the rotor moved further towards the landing deck, the rate of change in thrust gradually increased under the strengthening disturbance of the ship airwake on the rotor inflow, with a minimum thrust occurring close to the stern. Interestingly, the rotor thrust increased again just before the rotor reached the HOD position, suggesting a ground effect was present before the rotor got close enough for the downwash from the hangar wall recirculation to start weakening this thrust benefit.

In contrast to the rotor thrust, the pitching moment did not change significantly until the rotor hub crossed the stern and entered the landing deck area, where the pitch-down moment increased more rapidly and reached a maximum magnitude at the HOD position. Based on previous results (see Fig. 17(a)), the pitching moment was relatively insensitive to the location where the ship airwake impinged on the rotor. This again suggested that the variation in pitching moment was more dependent on the proximity and recirculation effect from the ship deck and the hangar wall. These phenomena likely contributed to the imbalance in thrust distribution about the pitch axis during the stern approach.

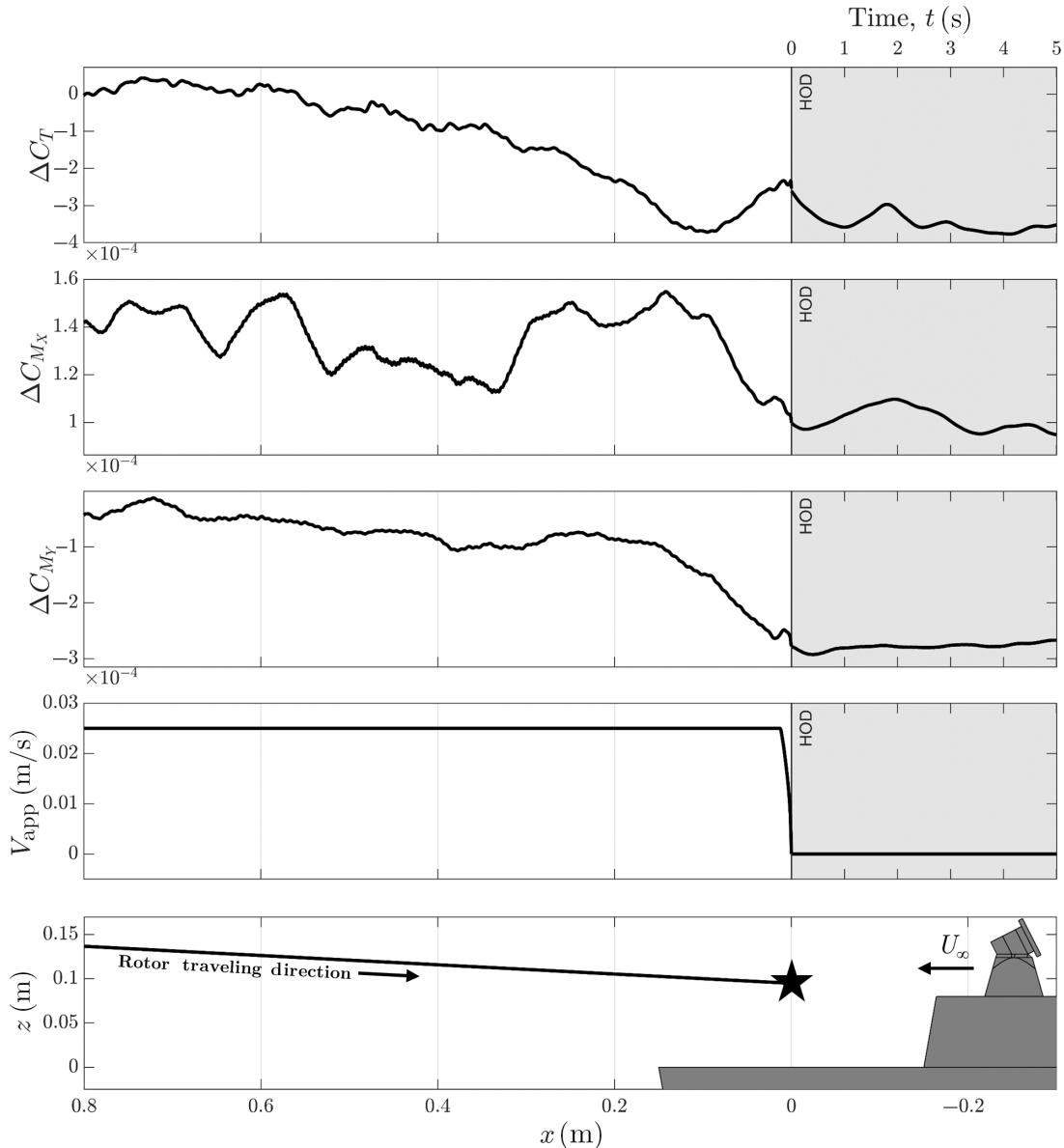


Fig. 27. History of the change in thrust and moment coefficients, approach velocity, and rotor position of the dynamically approaching rotor in headwind. (The Star symbol denotes the HOD position.)

Figure 28 shows the concurrent PIV flow field realizations and surface pressures at different rotor locations prior to the rotor reaching the HOD position. Flow fields and pressure contours were calculated using a sliding average function with a window length of 0.1 s centered at each target time instance. This corresponded to an averaging sample size of 11 for PIV and 81 for the pressures. From the pressure contour, the effect of the rotor wake was initially minimal and gradually increased as the rotor approached. The early-stage high-pressure zones on the deck were skewed towards the starboard side of the ship when at $x = 0.15$ and $x = 0.1$ m. However, this pattern shifted towards a port-side skew when the rotor reached $x = 0.05$ m and also towards the center of the landing deck. This shift likely caused the sudden change in the rolling moment right after the rotor entered the deck area.

From the PIV flow fields, a noticeable evolution of the rotor wake structure can be seen due to the mutual interactions between the rotor and the ship deck as the rotor approached the deck. The rotor wake was mostly uninterrupted at $x = 0.15$ m, even though half of the rotor disk was

already directly above the landing deck, owing to the high wake skew, which was estimated to be about 60 deg from simple momentum theory for forward flight given in Leishman (Ref. 31). As the rotor moved further in towards the landing deck, to $x = 0.1$ m and $x = 0.05$ m, the ship deck started to increasingly affect the upwind side of the rotor disk reducing the rotor wake velocity and skew angle. In addition, the downwind side of the rotor, although further away from the deck, exhibited a significant increase both in the wake velocity and skew angle when translating from $x = 0.1$ to $x = 0.05$ m. This was an indirect influence from the ship deck due to the wake from the upwind side of the rotor impinging the deck surface and being partially diverted downstream and off the landing deck. After reaching the HOD position at $x = 0$ m, the recirculation behind the hangar wall redirected a greater portion of the wake from the windward half of the rotor towards the hangar. This further intensified the recirculation and negatively affected the rotor inflow, which likely contributed to the rapid increase in the pitch-down moment due to half of the rotor ingesting greater downwash.

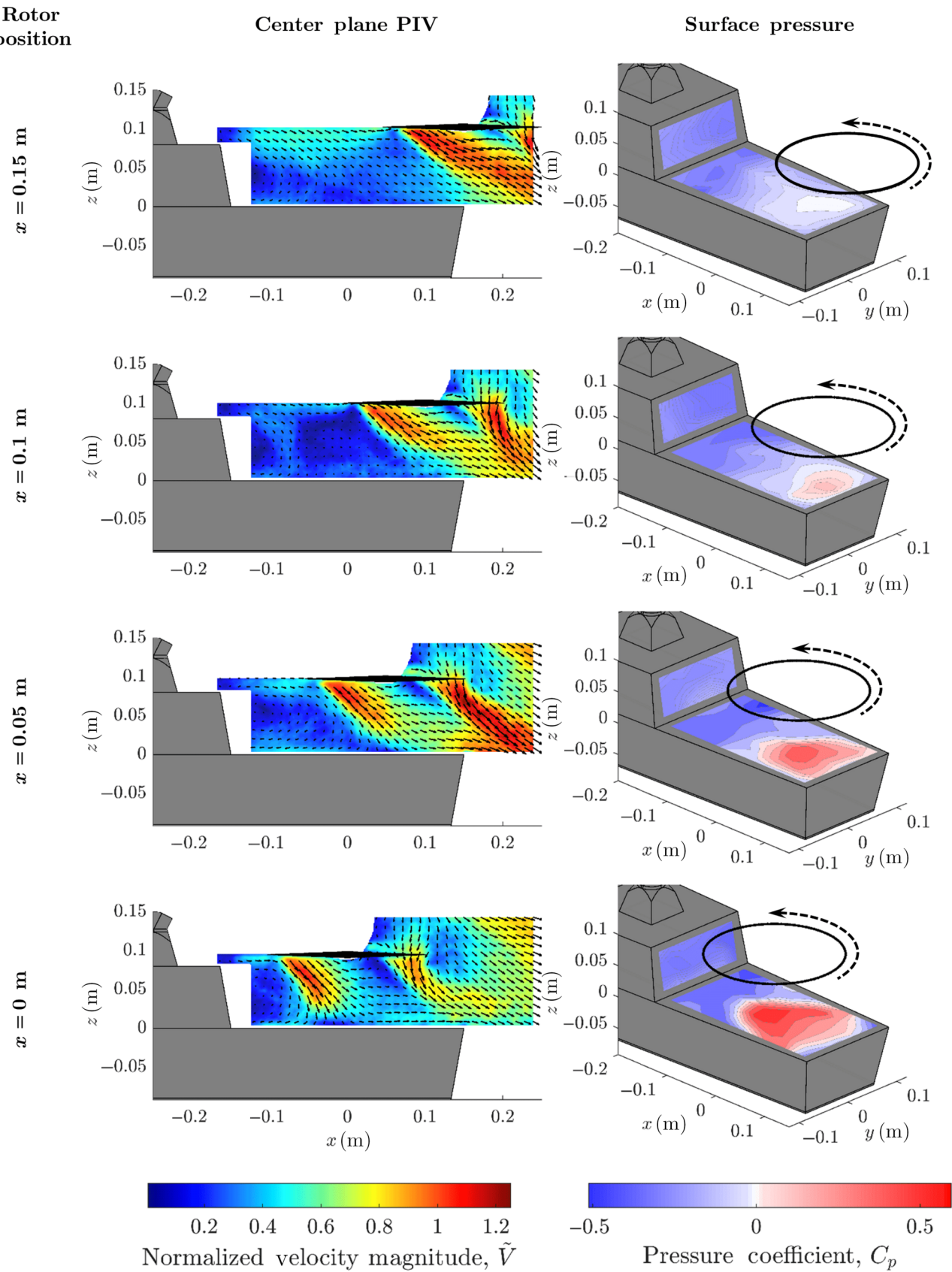


Fig. 28. Dynamic approach: Sliding average of normalized velocity magnitude at the longitudinal center plane of rotor/ship, and ship deck surface pressure distribution with the rotor at various positions prior to reaching the HOD position. (The rotor is indicated in black. Every eighth vector is shown.)

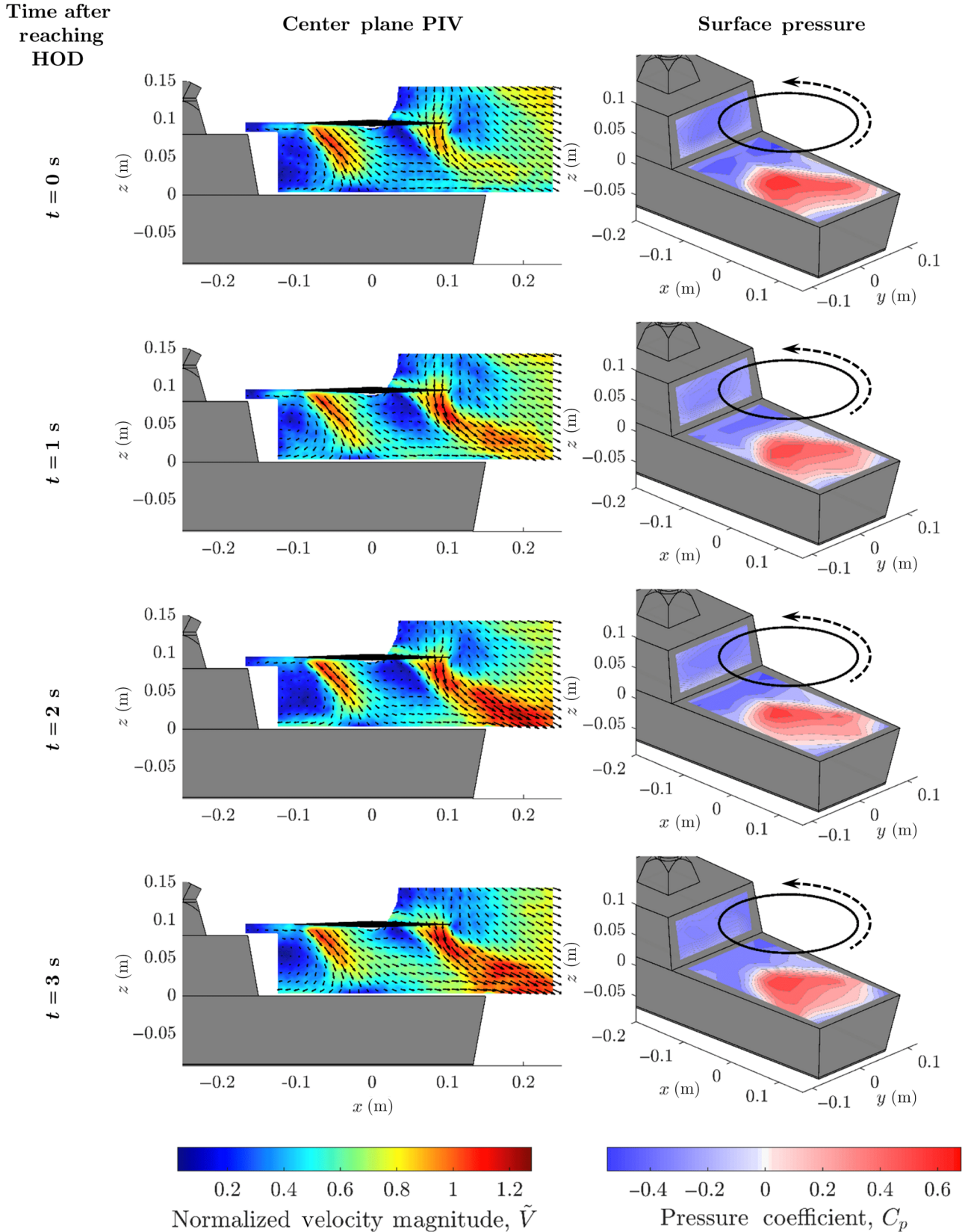


Fig. 29. Dynamic approach: Sliding average of normalized velocity magnitude at the longitudinal center plane of rotor/ship, and ship deck surface pressure distribution at time instances after the rotor has reached the HOD position. (The rotor is indicated in black. Every eighth vector is shown.)

After arriving at the hover-over-deck position, Fig. 27 shows that the rotor thrust and rolling moment experienced pronounced oscillatory fluctuations before converging and reaching equilibrium. The oscillation period of the rotor thrust was shorter and, at the same time, the magnitude dampened out slightly sooner than for the rolling moment (see Fig. 27). On the other hand, the pitching moment stayed relatively constant while the thrust and rolling moment were settling. From the flow fields and pressure distributions shown in Fig. 29, one can see that even after the rotor has reached the HOD position, the wake structure and ship deck pressure distribution continued to evolve over time and thus contributed to prolonged oscillations in the rotor hub loads. Using the acquired data, a more detailed comparison and correlation needs to be performed to better understand the relationship between the time history of rotor hub loads and the associated flow phenomena for the dynamically approaching rotor.

Conclusions

An extensive wind tunnel investigation of the ship–rotor dynamic interface problem between a 1:100 scale NATO-GD and a representative single main rotor under a 5 m/s freestream was performed in this study. The study involved an exploration of the effect of the rotor hub locations, WOD angles, and also dynamic rotor approach effects. Using concurrent measurements of rotor hub loads, ship deck surface pressures, and PIV flow field, a more detailed understanding of the underlying aerodynamic mechanisms and their effects on rotor hub loads was obtained. The following specific conclusions are drawn from this study:

1) The rotor thrust varied with the relative location to the ship and was mainly affected by the modified rotor inflow from the downwash induced by the recirculation near the hangar wall and also the cushioning effect from the separated flow along the windward side of the landing deck under higher WOD angles.

2) The variation in rotor rolling moments showed a strong dependency on the location where the ship airwake impacted the rotor disk, which altered the local rotor inflow and strongly correlated with the rotational direction of the rotor itself.

3) Impingement of the unsteady ship airwake on the retreating side of the rotor contributed to the majority of the unsteady RMS thrust. Additionally, due to the unique wake structure shed from the ship superstructure and the landing deck under higher WOD angles, a bifurcation in the region of high RMS thrust was observed under G30 wind.

4) The recirculation downstream of the hangar wall was intensified by the presence of the rotor hovering over the landing deck, which subjected the upwind half of the rotor disk to increased downwash velocity, inducing a large change in pitching moment.

5) Transient responses in rotor load measurements from the dynamically approaching rotor indicated a ground effect being effective prior to reaching the hover position and also showed continuous fluctuations in the rotor thrust and rolling moment while station-keeping after reaching the hover position.

The data and outcomes from the current research will be valuable for verifying and validating coupled ship–rotor(craft) simulations, which can then be used for analysis, pilot training, and investigating the ship helicopter operating limits.

Acknowledgments

This research was funded by the U.S. Government under Cooperative Agreement No. W911W6-21-2-0001. The U.S. Government is authorized to reproduce and distribute reprints for Government purposes notwithstanding any copyright notation thereon.

The views and conclusions contained in this document are those of the authors and should not be interpreted as representing the official

policies or position, either expressed or implied, of the U.S. Army Combat Capabilities Development Command (DEVCOM), Aviation & Missile Center (AvMC), or the U.S. Government.

Additionally, the authors would like to thank Abraham Atte, Howon Lee, Shreyas Srivathsan, and Dr. Sihong Yan for their assistance throughout the experimental campaigns and also Shreyas Ashok for his valuable input.

References

- ¹Zan, S. J., "Experimental Determination of Rotor Thrust in a Ship Airwake," *Journal of the American Helicopter Society*, Vol. 47, (2), April 2002, pp. 100–108, DOI: 10.4050/JAHS.47.100.
- ²Lee, R. G., and Zan, S. J., "Wind Tunnel Testing of a Helicopter Fuselage and Rotor in a Ship Airwake," *Journal of the American Helicopter Society*, Vol. 50, (4), October 2005, pp. 326–337, DOI: 10.4050/1.3092869.
- ³McTavish, S., Wall, A., and Lee, R., "A Methodology to Correlate Simulated Airwake Data and Unsteady Helicopter Load Measurements to Shipboard Helicopter Flight Test Data," Proceedings of the 14th International Conference on Wind Engineering, Porto Alegre, Brazil, June 21–26, 2015.
- ⁴Silva, M. J., Yamauchi, G. K., Wadcock, A. J., and Long, K. R., "Wind Tunnel Investigation of the Aerodynamic Interactions Between Helicopters and Tiltrotors in a Shipboard Environment," Proceedings of the American Helicopter Society 4th Decennial Specialist's Conference on Aeromechanics, San Francisco, CA, January 21–23, 2004.
- ⁵Wang, Y., Curran, J., Padfield, G., and Owen, I., "AirDyn: An Instrumented Model-Scale Helicopter for Measuring Unsteady Aerodynamic Loading in Airwakes," *Measurement Science and Technology*, **22**, 045901 (2011), DOI: 10.1088/0957-0233/22/4/045901.
- ⁶Kääriä, C. H., Wang, Y., White, M. D., and Owen, I., "An Experimental Technique for Evaluating the Aerodynamic Impact of Ship Superstructures on Helicopter Operations," *Ocean Engineering*, Vol. 61, 2013, pp. 97–108, DOI: 10.1016/j.oceaneng.2012.12.052.
- ⁷Silva, M., Schatzman, D., and Ramasamy, M., "Sub-Scale Investigation of Coupled Rotor/ Upwind Ship Aerodynamic Interactions," Proceedings of the 6th Decennial VFS Aeromechanics Specialists' Conference, Santa Clara, CA, February 6–8, 2024.
- ⁸Zhu, N., Zhang, Z., Gnanamanickam, E. P., and Leishman, J. G., "Estimation of 3D Ship Airwakes Using Dual-Plane PIV," *Experiments in Fluids*, Vol. 65, (1), 11, 2024, DOI: 10.1007/s00348-023-03727-3.
- ⁹Mazzilli, G. A., Zhu, N., Zhang, Z., Gnanamanickam, E. P., and Leishman, J. G., "Investigation of the Ship Airwake Bistable Recirculation Region," AIAA 2024-2385, Proceedings of the AIAA SciTech 2024 Forum, Orlando, FL, January 8–12, 2024, DOI: 10.2514/6.2024-2385.
- ¹⁰Palm, K. H., Zhang, Z., Gnanamanickam, E. P., and Leishman, J. G., "Behavior of Ship Airwakes Under Quartering Wind Conditions," AIAA 2024-2386, Proceedings of the AIAA SciTech 2024 Forum, Orlando, FL, January 8–12, 2024, DOI: 10.2514/6.2024-2386.
- ¹¹Nacakli, Y., Landman, D., and Doane, S., "Investigation of Backward-Facing-Step Flow Field for Dynamic Interface Application," *Journal of the American Helicopter Society*, **57**, 032005 (2012), DOI: 10.4050/JAHS.57.032005.
- ¹²Taymourtash, N., Zagaglia, D., Zanotti, A., Muscarello, V., Giberti, G., and Quaranta, G., "Experimental Study of a Helicopter Model in Shipboard Operations," *Aerospace Science and Technology*, **115**, 106774 (2021), DOI: 10.1016/j.ast.2021.106774.
- ¹³Oates, B., Kurban, E., Smith, M., and Rauleder, J., "Evaluation of High- and Mid-Fidelity Computational Fluid Dynamics for Complex

Ship Airwake Analysis with New Experimental Data," Proceedings of the 79th Annual Forum of the Vertical Flight Society, West Palm Beach, FL, May 16–18, 2023, DOI: 10.4050/F-0079-2023-17973.

¹⁴Forrest, J., Kaaria, C., and Owen, I., "Evaluating Ship Superstructure Aerodynamics for Maritime Helicopter Operations through CFD and Flight Simulation," *The Aeronautical Journal*, Vol. 120, (1232), 2016, pp. 1578–1603, DOI: 10.1017/aer.2016.76.

¹⁵Owen, I., Lee, R., Wall, A., and Fernandez, N., "The NATO Generic destroyer—A Shared Geometry for Collaborative Research into Modelling and Simulation of Shipboard Helicopter Launch and Recovery," *Ocean Engineering*, **228**, 108428 (2021), DOI: 10.1016/j.oceaneng.2020.108428.

¹⁶Fernandez, N., Watson, N., Owen, I., and White, M., "A Comparative Assessment of the NATO-GD and SFS2 Ship Airwakes and Their Influence upon Helicopter Aerodynamic Loading," Proceedings of the 78th Annual Forum of the Vertical Flight Society, Fort Worth, TX, May 10–12, 2022, DOI: 10.4050/F-0078-2022-17584.

¹⁷Owen, I., Fernandez, N., Lee, R., Wall, A., and Butler, J., "Modeling and Simulation of Shipboard Launch and Recovery of Helicopters—An Overview of AVT-315," AIAA 2023-4198, Proceedings of the AIAA Aviation 2023 Forum, San Diego, CA, June 12–16, 2023, DOI: 10.2514/6.2023-4198.

¹⁸Ashok, S. G., and Rauleder, J., "Mid-Fidelity NATO Generic Destroyer Static and Moving-Ship Airwake Simulations Using the Lattice-Boltzmann Method Compared with Experimental Data," *Ocean Engineering*, **298**, 117264 (2024), DOI: 10.1016/j.oceaneng.2024.117264.

¹⁹Fernandez, N., Wall, A., Owen, I., Lee, R., Yuan, W., and White, M. D., "Helicopter Aerodynamic Loading in the Airwake of a Moving Ship," Proceedings of the 79th Annual Forum of the Vertical Flight Society, West Palm Beach, FL, May 16–18, 2023, DOI: 10.4050/F-0079-2023-18122.

²⁰Hodge, S. J., Zan, S. J., Roper, D. M., Padfield, G. D., and Owen, I., "Time-Accurate Ship Airwake and Unsteady Aerodynamic Loads Modeling for Maritime Helicopter Simulation," *Journal of the American Helicopter Society*, **54**, 022005 (2009), DOI: 10.4050/JAHS.54.022005.

²¹Polsky, S. A., Wilkinson, C., Nichols, J., Ayers, D., Mercado-Perez, J., and Davis, T. S., "Development and Application of the SAFEDI Tool

for Virtual Dynamic Interface Ship Airwake Analysis," AIAA 2016-1771, Proceedings of the 54th AIAA Aerospace Sciences Meeting, San Diego, CA, January 4–8, 2016, DOI: 10.2514/6.2016-1771.

²²Ashok, S. G., and Rauleder, J., "Towards Real-Time Coupled Ship-Rotorcraft Interactional Simulations Using GPU-Accelerated Lattice-Boltzmann Method," Proceedings of the 80th Annual Forum of the Vertical Flight Society, Montreal, Canada, May 7–9, 2024, DOI: 10.4050/F-0080-2024-1346.

²³NATO AVT-315 Task Group, "Comparative Assessment of Modelling and Simulation Methods of Shipboard Launch and Recovery of Helicopters," Technical Report STO-TR-AVT-315, 2023, DOI: 10.14339/STO-TR-AVT-315.

²⁴Healey, J. V., "Establishing a Database for Flight in the Wakes of Structures," *Journal of Aircraft*, Vol. 29, (4), 1992, pp. 559–564, DOI: 10.2514/3.46202.

²⁵Rosenfeld, N., Kimmel, K., and Sydney, A. J., "Investigation of Ship Topside Modeling Practices for Wind Tunnel Experiments," AIAA 2015-0245, Proceedings of the 53rd AIAA Aerospace Sciences Meeting, Kissimmee, FL, January 5–9, 2015, DOI: 10.2514/6.2015-0245.

²⁶Adatrao, S., and Sciacchitano, A., "Elimination of Unsteady Background Reflections in PIV Images by Anisotropic Diffusion," *Measurement Science and Technology*, **30**, 035204, (2019), DOI: 10.1088/1361-6501/aafca9.

²⁷McRuer, D. T., "Interdisciplinary Interactions and Dynamic Systems Integration," *International Journal of Control*, Vol. 59, (1), 1994, pp. 3–12, DOI: 10.1080/00207179408923067.

²⁸Barlow, J. B., Rae, W. H., and Pope, A., *Low-Speed Wind Tunnel Testing*, John Wiley & Sons, New York, NY, 1999, p. 374.

²⁹Taylor, G. I., "The Spectrum of Turbulence," Proceedings of the Royal Society of London. Series A - Mathematical and Physical Sciences, Vol. 164, (919), 1938, pp. 476–490, DOI: 10.1098/rspa.1938.0032.

³⁰Deng, S., Percin, M., and van Oudheusden, B., "Experimental Investigation of Aerodynamics of Flapping-Wing Micro-Air-Vehicle by Force and Flow-Field Measurements," *AIAA Journal*, Vol. 54, (2), 2016, pp. 588–602, DOI: 10.2514/1.J054403.

³¹Leishman, G. J., *Principles of Helicopter Aerodynamics*, Cambridge University Press, New York, NY, 2006, p. 160.